Title: Differential migration mechanics and immune responses of glioblastoma subtypes

Authors: Ghaidan A. Shamsan[1], Chao J. Liu[1,11], Brooke C. Braman[1], Susan K. Rathe[2], Aaron L. Sarver[2,3], Nima Ghaderi[4], Mariah M. McMahon[1], Rebecca L. Klank[1], Barbara R. Tschida[2], S. Joey McFarren[2], Pamela C. Rosato[5,12], David Masopust[5], Jann N. Sarkaria[6], H. Brent Clark[7], Steven S. Rosenfeld[8+], David A. Largaespada[2,9+], David J. Odde[10+]

Affiliations:
[1] Department of Biomedical Engineering, University of Minnesota, Minneapolis, MN 55455
[2] Masonic Cancer Center, University of Minnesota, Minneapolis, MN 55455
[3] Institute for Health Informatics, University of Minnesota, Minneapolis, MN 55455
[4] Department of Mechanical Engineering, University of Minnesota, Minneapolis, MN 55455
[5] Department of Microbiology and Immunology, Center for Immunology, University of Minnesota, Minneapolis, MN, 55455
[6] Department of Radiation Oncology, Mayo Clinic, Rochester, MN, 55902
[7] Laboratory Medicine and Pathology, University of Minnesota, Minneapolis, MN 55455
[8] Department of Molecular Pharmacology and Experimental Therapeutics, Mayo Clinic, Jacksonville, FL 32224
[9] Department of Pediatrics, University of Minnesota, Minneapolis, MN 55455
[10] Department of Biomedical Engineering, University of Minnesota, Minneapolis, MN 55455, USA. Electronic address: oddex002@umn.edu.
[11] Present address: Athinoula A. Martinos Center for Biomedical Imaging, Department of Radiology, Massachusetts General Hospital/Harvard Medical School, Charlestown, MA 02129
[12] Present address: Department of Microbiology and Immunology, The Geisel School of Medicine at Dartmouth, Lebanon, NH 03756
[+] co-senior authors

SUMMARY:

Glioblastoma remains a deadly cancer driven by invasion of tumor cells into the brain. Transcriptomic analyses have revealed distinct molecular subtypes, but mechanistic differences that explain clinical differences are not clear. Here, we show that, as predicted by the motor-clutch model for cell migration, mesenchymal glioma cells are more spread, generate larger traction forces, and migrate faster in brain tissue compared to proneural cells. Despite their fast migration and comparable proliferation rate in vitro, mice with mesenchymal tumors live longer than mice with proneural tumors, which was correlated with an immune response in the mesenchymal mice that included T cell-mediated killing of cancer cells, similar to human tumors. Thus, mesenchymal tumors have aggressive migration, but are relatively immunologically ‘hot’ which suppresses net proliferation. These two features counteract each other and may explain the lack of a strong survival difference between subtypes clinically, while also opening up new opportunities for subtype-specific therapies.

INTRODUCTION:

Glioblastoma (GBM: WHO grade IV primary brain tumor) progression can be characterized in terms of tumor growth and spreading, two key parameters which are influenced by many of the hallmarks of cancer (Hanahan and Weinberg, 2011). In GBM, tumor spreading is driven by tumor cells' ability to infiltrate healthy brain parenchyma, which prevents complete surgical resection and results in tumor recurrence (de Gooijer et al., 2018; Hoelzinger et al., 2007; Lefranc et al., 2005). Molecular and genetic analyses of human GBM have identified at least three distinct molecular subtypes: proneural, classical, and mesenchymal (Phillips et al., 2006; Verhaak et al., 2010; Wang et al., 2017). These subtypes were shown to strongly correlate with specific genetic alterations (Mesenchymal: *NF1* loss; Classical: *EGFRvIII*; Proneural: *PDGFRA*) and cellular developmental states (Neftel et al., 2019; Patel et al., 2014; Verhaak et al., 2010; Wang et al., 2017). Despite accumulating evidence of distinct transcriptomic and genetic signatures, the characteristic mechanistic differences between such signatures, if any, have not been identified. As a result, it remains unclear how knowledge of the different subtypes should inform clinical decisions.

One intriguing correlate of subtype is the level of CD44 expression, a cell surface protein expressed on tumor and immune cells, which is known to play a role in cancer progression across a variety of cancers including GBM (Bhat et al., 2013; Klank et al., 2017; Mao et al., 2013; Mooney et al., 2016; Naor et al., 2002; Neftel et al., 2019; Ozawa et al., 2014; Pietras et al., 2014; Toole, 2009; Wang et al., 2017). In GBM, we previously showed that CD44 expression is a prognostic marker with a biphasic dependence: better outcomes are observed at both lower and higher levels of CD44

while poorer outcomes are observed at intermediate levels, an example of optimality and the 'goldilocks' phenomenon (Klank et al., 2017). In animal models, CD44 expression has further been shown to correlate with glioma cell migration in a biphasic relationship with a peak migration rate at intermediate expression level, which also correlated with the minimum in survival in both the animal model and human GBM (Klank et al., 2017). In addition, *CD44* transcript levels are shown to vary across GBM molecular subtypes with elevated expression in mesenchymal tumors (Phillips et al., 2006; Pietras et al., 2014; Verhaak et al., 2010). *CD44* expression in the mesenchymal tumors is, on average, closer to the *CD44* level that corresponds to the minimum in patient survival than the proneural subtype (Klank et al., 2017). As an adhesion molecule, CD44 engages the extracellular matrix with the actin cytoskeleton through adapter proteins to mediate cell migration (Toole, 2009). This suggests that mesenchymal cells have a near-optimal level of CD44 adhesion molecules to serve as molecular "clutches" that resist myosin II motor forces, allowing them to migrate faster than proneural cells which on average have a lower, suboptimal level of CD44 clutches (see Figure 2B and 4E in Klank *et al.,* 2017). This could then explain the slightly worse outcomes for mesenchymal patients and higher cell migration and invasion (Wang et al., 2017; Yoshida et al., 2012). In addition, it would predict that mesenchymal cells would have lager cellular spread area, be more polarized, and generate more traction force as they migrate. More generally, lower CD44 is indicative of an epithelial state and higher CD44 indicative of a mesenchymal state (Bloushtain-Qimron et al., 2008; Polyak and Weinberg, 2009), and so an increase in myosin motors and adhesions, either

integrin- or CD44-mediated, may be driving the epithelial-to-mesenchymal transition (EMT) in a variety of cancers such as breast cancer (Mekhdjian et al., 2017).

Based on these previous results, we tested the hypothesis that a key mechanistic difference between GBM molecular subtypes is that proneural cells are slow migrating and mesenchymal cells are fast migrating. To address this question, we generated animal models recapitulating the transcriptomic signatures of human mesenchymal and proneural GBM in an immune competent background using perturbations of known GBM oncogenic pathways. Specifically, mesenchymal and proneural-like tumors were driven by SV40-large T (LgT) antigen, to mimic common inhibition of p53 and Rb signaling found in GBM (Ahuja et al., 2005; McLendon et al., 2008), in combination with either $NRAS^{G12V}$ (NRAS) or PDGFB (PDGF), respectively, which resulted in mesenchymal or proneural transcriptomic features with only a single genetic change required to switch subtypes in a wild type mouse background. As predicted, *CD44* expression was higher in NRAS-driven tumors and, consistent with our simulation predictions, *ex vivo* brain slice live imaging showed NRAS tumor cells migrate faster than PDGF tumor cells, and exhibit greater spreading, polarization, and force generation as well. Despite increased migration, the NRAS cohort had better survival than PDGF which was attributed to enhanced antitumoral immune response in NRAS tumors, consistent with increased immune cell infiltration in human mesenchymal GBM (Doucette et al., 2013; Hara et al., 2021; Wang et al., 2021, 2017). Overall our work identified a clinically actionable difference in migration mechanics between GBM subtypes and establishes an integrated biophysical modeling and experimental

115 approach to mechanically parameterize and simulate distinct molecular subtypes in

116 preclinical models of cancer.

RESULTS:

Genetically induced high-grade glioma mouse models recapitulate the transcriptomic signatures of mesenchymal and proneural GBM

To characterize the mechanics of GBM subtypes, we utilized the *Sleeping Beauty* (SB) transposon-based gene transfer system to induce high grade gliomas in immunocompetent FVB/NJ-strain mice (Calinescu et al., 2015; Klank et al., 2017; Koschmann et al., 2016; Núñez et al., 2019; Wiesner et al., 2009). Constructs of plasmids carrying SB transposons with oncogenic driver transgenes (SV40-LgTA+NRAS^{G12V} or SV40-LgTA+PDGFB; here termed NRAS and PDGF, respectively) were used to model mesenchymal and proneural GBM tumors, respectively (Figure 1A). DNA plasmids carrying an SB transposon with encoded firefly luciferase and green fluorescent protein (GFP) transgenes, and expressing SB transposase were co-injected to allow for confirmation of successful gene transfer, detecting tumor development and monitoring tumor growth using bioluminescence imaging (BLI) and single cell tracking using fluorescence microscopy. Similar to human GBM, histological sections from these tumors exhibited highly mitotic tumor cells, necrosis, anaplasia, and perivascular infiltration and proliferation, (Figure 1B).

To assess whether the NRAS and PDGF tumors recapitulated the mesenchymal and proneural subtypes, respectively, we performed cross-species transcriptomic analysis using bulk RNA sequencing data from mouse and human tumors. Bulk RNA sequencing was performed on tumor tissues from both cohorts and on normal brain tissues (NBT) (NRAS N=4, PDGF N=4, and NBT N=3). IDH-WT human GBM transcriptomic profiles were retrieved from Broad GDAC Firebrowse (Brennan et al.,

2013). Unsupervised hierarchical clustering of the mouse dataset (Table S1) revealed clear differences between normal tissue and tumor tissue and between NRAS and PDGF tumors (Figure S1A). Not surprisingly, gene ontology enrichment analysis, using *EnrichR* (Kuleshov et al., 2016), showed an enrichment of cell cycle related processes in tumor tissue specific gene cluster (817 genes) (Figure S1B) and neuronal processes in normal tissue cluster (1722 genes) (Figure S1D). Interestingly, the NRAS-specific cluster (1327 genes) was enriched with cytokine-mediated signaling and inflammatory response processes (Figure S1C).

To determine whether any variations observed between the two mouse cohorts were also present in human tumors, unsupervised hierarchical clustering was performed on both mouse and human tumor datasets and clusters were independently identified in both datasets (Table S2). Three and 10 gene clusters were identified in both mouse and human datasets, respectively, as shown in Figure 1C. We identified mouse cluster MC1 (n=1534 genes) as being significantly enriched in genes found in human cluster HC1 (n=1186 genes, $p < 1x10^{-15}$), MC2 (n=414 genes) is significantly enriched in genes found in HC2 (n=1098 genes, $p < 1x10^{-15}$), and MC3 (n=232 genes) is significantly enriched in genes enriched in HC4 (n=432, $p < 1x10^{-15}$). These results show that conserved transcriptomic patterns distinguish subtypes of both mouse and human tumors.

To assess whether the transcriptional patterns present in the mouse tumor models represent previously described GBM subtypes, we compared the expression of identified mouse gene clusters within human GBM subtypes. We found that MC1, which is enriched in NRAS tumors, is significantly enriched in human mesenchymal GBM

relative to proneural and classical GBMs (Figure 1D). In contrast, MC3, which is enriched in PDGF tumors, is significantly enriched in proneural GBM relative to mesenchymal and classical GBMs (Figure 1D). Furthermore, we found the expression of known mesenchymal and proneural genes and gene signatures are relatively elevated in NRAS and PDGF tumors, respectively (Figure 1E, 1F and S2). These results demonstrate that NRAS and PDGF tumors transcriptionally resemble mesenchymal and proneural GBMs, respectively.

Motor-clutch modeling of cell migration predicts NRAS/Mesenchymal tumor cells will migrate faster, have larger cell spread area, and generate more force than PDGF/Proneural tumor cells

To examine tumor cell migration, we used our cell migration simulator (Bangasser et al., 2017; Klank et al., 2017) to predict migration phenotypes in response to gene expression changes. The cell migration simulator is based on the motor-clutch model which incorporates actin-based protrusion dynamics, mass conservation, and force balances to reproduce cell polarization and random motility in 1D and 2D compliant microenvironments (Bangasser et al., 2013, 2017; Chan and Odde, 2008; Estabridis et al., 2018; Hou et al., 2019; Klank et al., 2017; Liu et al., 2019; Prahl et al., 2018, 2020). The number of adhesion/clutches and motors are key determinants of cell migration, with a relative balance being essential for efficient migration (Bangasser et al., 2013, 2017; DiMilla et al., 1991). Using a set of 54 cell migration genes expressed in the human U251 GBM cell line (Bangasser et al., 2017), NRAS tumors significantly upregulate transcription of adhesion and adapter genes (Figure S3A). A similar set of genes was also significantly upregulated in MES relative to PN GBM (Figure S3B). Both

NRAS and MES tumors upregulated *CD44* and its cognate adhesion adapter gene moesin (*MSN*), which mechanically links the CD44 cytoplasmic tail to F-actin (Fehon et al., 2010; Freeman et al., 2018; Legg and Isacke, 1998; Ponta et al., 2003; Toole, 2009; Tsukita et al., 1994; Yonemura, 1998). Notably, the levels of myosin motor genes were not differentially expressed in the mouse dataset, while, in the human dataset, *MYH9* and *MYO1C* were modestly upregulated in MES tumors but to a lesser degree than adhesion molecules (Figure S3B). These results suggest NRAS/Mesenchymal tumor cells have a higher number of adhesion/clutches than PDGF/Proneural tumor cells and little to no change in the number of motors.

Based on these results, we simulated the effect of *CD44* expression level on cell migration by simply adjusting the number of adhesion bonds (number of clutches, N_c) in the model (Bangasser et al., 2017; Klank et al., 2017). We used low clutches relative to motors (low adhesion) to simulate PDGF/Proneural cells and a medium level of clutches that balanced the number of motors (optimal adhesion) to simulate NRAS/Mesenchymal cells (Figure 2A). Our simulations show that lowering the number of adhesions, representing the PDGF/Proneural case, results in reduced cell migration, force transmission, cell spread area, and cell polarization due to an insufficient number of clutches relative to the number of motors, as shown in Figure 2. In the case where the number of clutches and motors are balanced, representing the NRAS/Mesenchymal case, where the number of adhesions is increased while holding the number of motors constant, simulated cells recover their ability to migrate, transmit forces, spread, and polarize across a range of substrate stiffnesses. Consequently, simulation results predict that NRAS/Mesenchymal tumor cells will migrate faster than PDGF/Proneural

tumor cells due to increase of adhesion (i.e. CD44) expression in NRAS/Mesenchymal tumors and not due to small difference in molecular motor expression (Figure S3A and S3B). In addition, due to their higher number of clutches and balanced motor-clutch ratio, NRAS/Mesenchymal tumor cells are predicted to generate higher force, have larger spread area, and be more polarized.

NRAS/Mesenchymal tumor cells migrate faster than PDGF/Proneural tumor cells in brain tissue

To test our model prediction that NRAS/Mesenchymal cells migrate faster than PDGF/Proneural cells, we performed live cell imaging on tumor bearing mouse brain slices using confocal microscopy. Time-lapse images of GFP-positive tumor cells were used to track single cell migration and generate single cell trajectories. As shown in Figure 3A, 3B and Video S1, NRAS/Mesenchymal tumor cells appeared qualitatively to move farther, have larger spread area, and polarize to a greater extent than PDGF/Proneural tumor cells. Quantitative analysis of single cell trajectories confirmed that NRAS/Mesenchymal tumor cells have a higher random motility coefficient than PDGF/Proneural tumor cells (30.1 $\mu m^2\ hr^{-1}$ *vs* 2.5 $\mu m^2\ hr^{-1}$, $p<0.001$; see Figure 3C and S4A). In addition, morphological analysis of tumor cells revealed cell spread area and cell aspect ratio (i.e. polarization) are also higher in NRAS/Mesenchymal tumor cells than PDGF/Proneural tumor cells (406.6 μm^2 vs 235.8 μm^2, $p<0.00001$ and 2.1 *vs* 1.7, $p<0.001$, respectively, see Figure 3D, 3E, S4B and S4C). As predicted by our modeling, and the hypothesis that NRAS/Mesenchymal has balanced motors and clutches while PDGF/Proneural lacks sufficient clutches, we find NRAS/Mesenchymal cells migrate faster, are more spread, and are more polarized than PDGF/Proneural cells.

235

236 **Migration phenotype is species and tumor microenvironment independent**

237 To determine whether migration phenotype is cancer cell intrinsic as predicted by
238 our modeling and not due to microenvironment differences, we generated three primary
239 mouse lines grown as neurospheres from each cohort to investigate their migration
240 phenotype outside their tumor microenvironment. Organotypic mouse brain slice culture
241 was used to image tumor cell migration in healthy mouse brain slices (Liu et al., 2019).
242 Dissociated mouse tumor cells were plated and allowed to invade and migrate in
243 healthy mouse brain slices. Figure 4A shows representative fluorescence images of
244 primary isolated cells in organotypic slice culture. Time-lapse imaging was used to track
245 single cells and quantify their migration rates. Consistent with the *ex vivo* migration in
246 intact tumor-bearing brain slices, random motility coefficient in normal mouse brain
247 tissue is higher for primary NRAS/Mesenchymal tumor cells than primary
248 PDGF/Proneural tumor cells (131.4 $\mu m^2\ hr^{-1}$ *vs* 31.3 $\mu m^2\ hr^{-1}$, $p<0.00001$; Figure 4B,
249 S4D and Video S2). The area of cell spreading is also higher in primary
250 NRAS/Mesenchymal tumor cells than PDGF/Proneural (1075.1 μm^2 *vs* 838.8 μm^2,
251 $p<0.001$; Figure 4C and S4E). Furthermore, cell aspect ratio, the ratio of major and
252 minor axis of a fitted ellipse, was trending higher in NRAS/Mesenchymal tumor cells
253 than PDGF/Proneural but did not reach statistical significance (Figure 4D and S4F).
254 To assess the relevance of these results to human GBM, we tested the migration
255 phenotype of six patient-derived xenograft (PDX) lines (three mesenchymal and three
256 proneural) using the organotypic mouse brain slice culture. Figure 4E shows
257 representative fluorescence images of PDX cells in organotypic slice culture. We found

mesenchymal PDX cells migrate faster than proneural PDX cells (43. $\mu m^2\ hr^{-1}$ *vs* 8.8 $\mu m^2\ hr^{-1}$, p<0.00001; Figure 4F, S4G and Video S3). In addition, similar to our mouse models, mesenchymal PDX cells have larger area of cellular spreading and aspect ratio relative to proneural PDX cells (701.7 μm^2 vs 564.6 μm^2, p<0.00001 and 2.3 *vs* 2.0, p<0.001, respectively, see Figure 4G, S4H, 4H and S4I).

Traction strain energy is larger for NRAS/Mesenchymal cells than for PDGF/Proneural cells, consistent with model predictions

In addition, cell migration simulations predict NRAS/Mesenchymal tumor cells would have increased force generation as a result of higher number of clutches resulting in balanced myosin motors and clutches, relative to PDGF/Proneural tumor cells which would have insufficient clutches relative to motors (Figure 2D). Using the primary isolated mouse lines, traction force microscopy was used to measured traction strain energy generated by tumor cells on polyacrylamide hydrogels (Bangasser et al., 2017; Butler et al., 2002). Because transcriptomic analysis showed an overall higher level of adhesion molecules in NRAS/Mesenchymal tumor tissues, including CD44 and integrins, Type-I Collagen was used to coat polyacrylamide hydrogels (Figure S3A). Because of the overall higher level of adhesion Consistent with model predictions, NRAS/Mesenchymal tumor cells generate higher traction strain energy than PDGF/Proneural tumor cells across different substrate Young's moduli (Figure 5A and 5B). Cell spread area is also higher in NRAS/Mesenchymal than PDGF/Proneural on polyacrylamide hydrogels (Figure 5C). In addition, NRAS/Mesenchymal cells exhibit stiffness sensitive cell spreading; cells on stiff substrate (4.6 and 9.3 kPa) were more

spread than on soft substrate (0.7kPa, p <0.00001; see Figure 5C). Furthermore, we also examined force generation of mesenchymal and proneural PDX cells in mouse brain slices. Qualitative analysis of vasculature deformation is consistent with the model prediction that mesenchymal PDX cells generate larger deformations relative to proneural PDX cells, as shown in Figure 5D, 5E and Video S3.

NRAS/Mesenchymal mice have better survival and slower tumor growth rate

Since NRAS/Mesenchymal cells have nearly optimal *CD44* expression, and therefore higher motility compared to PDGF/Proneural cells which have a suboptimal low level of *CD44* expression (Klank et al., 2017), we asked whether the differences in migration rate, morphology and force generation correlate with disease progression and survival. Specifically, based on the faster migration in the NRAS/Mesenchymal cohort, we expected that these mice would progress faster and die sooner than PDGF/Proneural mice. To test this hypothesis, we measured survival times of tumor bearing mice and found that, opposite to our expectation, the NRAS/Mesenchymal cohort had better median survival than PDGF/Proneural cohort (NRAS N=21, PDGF N=24, 65 days vs. 35 days, log-rank test, p<0.0001; Figure 6A). To explain the difference in survival, we quantified *in vivo* tumor growth using bioluminescence imaging (BLI) of tumor-bearing mice. Consistent with their shorter survival, we found PDGF tumors grew twice as fast as NRAS tumors (Slopes: 0.127±0.01191 vs. 0.0716±0.00343 p <0.001, Figure 6B and 6C). Using mouse tumor neurospheres, we quantified mouse primary tumor cell line proliferation rates *in vitro* and found no significant difference between NRAS/Mesenchymal and PDGF/Proneural cells (Figure 6D). These results

imply that an additional factor, besides proliferation or migration, enables the NRAS/Mesenchymal mice to live longer and their tumors to grow slower *in vivo* than PDGF/Proneural mice.

NRAS/Mesenchymal mice have increased immune response relative to PDGF/Proneural mice

Because mesenchymal GBMs are known to be relatively immunologically "hot" – which presumably confers a survival benefit due to an antitumoral immune response- relative to immunologically "cold" proneural GBMs (Doucette et al., 2013; Neftel et al., 2019; Wang et al., 2017), we assessed the extent to which mouse NRAS/Mesenchymal tumors induce an immunological response relative to PDGF/Proneural tumors and normal brain tissues. Using our mouse transcriptomic dataset and previously published GBM immune gene sets (Doucette et al., 2013), NRAS/Mesenchymal tumors were found to have increased expression of both immune activators and suppressors gene signatures similar to human mesenchymal GBM (Doucette et al., 2013), as shown in Figure 7A and 7B. Specifically, expression of immune cell marker genes such as *Aif1*, *Itgam* (microglia/macrophages) and *Cd3* (T cells) are elevated in NRAS/Mesenchymal tumors relative to PDGF/Proneural tumors (Figure 7C upper panel) and in mesenchymal GBMs relative to proneural and classical GBMs (Figure 7C lower panel). Elevated expression of immune cell markers is indicative of increased immune cell infiltration in mesenchymal tumors. Consistent with the transcriptomic findings, IHC staining of NRAS/Mesenchymal and PDGF/Proneural tumor sections revealed significant levels of immune cell infiltration, including both microglia/macrophages and

T-lymphocytes, in NRAS/Mesenchymal but much less so in PDGF/proneural tumors (Figure 7D). Furthermore, increased immune infiltration and activity in NRAS/Mesenchymal tumors was accompanied by increased cell killing as measured by granzyme B and cleaved caspase-3 staining (Figure 7D). Image clustering analysis was used to quantify CD3, IBA1, granzyme B, and cleaved caspase-3 staining, and statistically significant differences were observed between NRAS/Mesenchymal and PDGF/Proneural cohorts (Figure 7E-H). This anti-tumor response was also evident in the three instances where NRAS mice developed tumors and tumor regression was observed (Figure S5). Despite the anti-tumor immune response observed in NRAS/Mesenchymal tumors, transcriptomic analysis also revealed elevated relative expression of immune checkpoint genes including PDL1, CTLA4, and CD200R1 (Figure S6). Thus, the NRAS/mesenchymal tumors, like human mesenchymal GBMs, are relatively immunologically “hot” with evidence of both immune activation and immune suppression, as well as evidence of cell killing. Altogether, the enhanced immune cell-associated tumor cell killing provides a mechanism by which survival is extended in NRAS/Mesenchymal tumors despite their enhanced migration speeds relative to PDGF/Proneural tumors.

Brownian dynamics simulations explain NRAS/Mesenchymal and PDGF/Proneural tumor progression

To quantitatively describe the interplay between tumor cell migration and proliferation and anti-tumoral immune response in tumor growth, we developed a three-dimensional (3D) Brownian dynamics tumor simulator (BDTS) based on our original 1D

Brownian dynamics simulator (Klank et al., 2018; Ray et al., 2018). The simulator takes into account anti-tumoral immune cells that infiltrate tissue, migrate, proliferate, encounter cancer cells, deliver cytotoxic agents, dissociate from cancer cells, undergo exhaustion, and, eventually, undergo apoptosis (or egress to lymphatics) as shown in Figure 8A. At the same time, cancer cells migrate, proliferate and undergo CTL-mediated death in the presence of anti-tumoral immune cells in the case NRAS/Mesenchymal tumors. In the case of PDGF/Proneural tumors, no anti-tumoral immune cells were simulated. Figure 8B shows simulation output at day 0 and day 16, which showed the observed behavior of overall faster growth of PDGF/Proneural tumors. In the NRAS/Mesenchymal tumor simulations, cancer cells appear more dispersed, whereas, in PDGF/Proneural simulations, cancer cells are less dispersed. Simulated tumor growths were plotted in Figure 8C and shown in Video S4. Using the parameters in Table S5, including the experimentally observed single cell migration speeds and neurosphere proliferation rates, simulated tumors qualitatively recapitulate the *in vivo* growth profile of NRAS/Mesenchymal and PDGF/Proneural tumors without parameter adjustment (Figure 8C).

DISCUSSION:

Understanding glioma progression and the mechanism driving glioma cell migration is critical for the design of effective therapies. Here we developed high-grade glioma mouse models which capture the transcriptomic and the immune microenvironment changes associated with human proneural and mesenchymal GBMs. Using the mouse models and PDX lines, we defined a mechanistic difference in glioma cell migration which highlights a functional characteristic of GBM molecular subtypes. The migration difference was consistent with changes in cellular adhesion, notably by *CD44*, but not molecular motors such as myosin II motors. This finding points toward an anti-migratory therapy approach targeted against cellular adhesion as opposed to myosin motors. With the negative Phase III clinical trial of the integrin-inhibitor, Cilengitide for GBM (Stupp et al., 2014), it is possible that integrins may not be the major adhesion molecules utilized by glioma cells to migrate but instead they could utilize CD44. While anti-CD44 therapies have not been tried in GBM, an anti-CD44 monoclonal antibody therapy (RO5429083, Roche, Basel, Switzerland) has been investigated in Phase I trials in patients with solid tumors and with AML (Menke-van der Houven van Oordt et al., 2016; Vey et al., 2016). Therefore, an anti-CD44 therapy could provide clinical benefits by slowing glioma migration.

Furthermore, the upregulation of CD44 in mesenchymal tumors is supportive of the existing literature which defines CD44 as a marker of cancer stem cell and EMT (Bloushtain-Qimron et al., 2008; Polyak and Weinberg, 2009; Ponta et al., 2003). During EMT, cancer cells take a more mesenchymal migratory phenotype to allow them to

migrate through dense ECM and metastasize (Chaffer and Weinberg, 2011). Our results associate enhanced migration in mesenchymal glioma cells with increased traction forces due to increased adhesion molecules expression 'clutches' such as CD44. Similarly, in breast cancer cells, TGF-β-induced EMT is associated with increased traction forces and clutch number (Mekhdjian et al., 2017). Interestingly, downregulation of NF1, a negative regulator of Ras, in epithelial breast cancer cells and Schwann cells also induces expression of transcription factors related to EMT (Arima et al., 2010). Moreover, in our study, $NRAS^{G12V}$ expression was used to mimic NF1 downregulation and inactivation in mesenchymal GBM (Krusche et al., 2016; Verhaak et al., 2010). Ras hyperactivation of MAPK pathway is required for EMT but not PI3K activation by Ras (Janda et al., 2002). Altogether, our results implicate EMT in enhanced glioma cell migration and force transmission associated with increased molecular clutches through, and suggest upregulation of clutches, either integrins or CD44, as a conserved feature of EMT across a range of cancers.

Despite the faster migration of the NRAS/Mesenchymal cells, the anti-tumoral immune response within the NRAS/Mesenchymal mouse model is able to slow disease progression and improve survival despite enhanced migration relative to the PDGF/Proneural mouse model. Such an anti-tumor response could potentially be used to slow disease progression and improve clinical outcome for GBM patients. In both mouse and human GBM, mesenchymal tumors are immunologically 'hot' relative to the immunologically 'cold' proneural tumors (Doucette et al., 2013; Wang et al., 2017). Despite the presence of immune cells within mesenchymal tumors, immune suppression leads to tumors ultimately prevailing against the anti-tumoral immune

response. Based on these findings, we propose an immune checkpoint inhibition strategy, in combination with an anti-migratory therapy, targeting mesenchymal GBM but not proneural GBM.

Our study utilizes an integrated, state of the art experimental approach to study GBM progression and model GBM molecular subtypes by switching a single oncogenic driver ($NRAS^{G12V} \leftrightarrow$ PDGFB), in an immunocompetent background without the need for genetically engineered mouse strains or further breeding. Using live cell and brain slice imaging, we identify key mechanical differences between mesenchymal and proneural tumor cells, with mesenchymal cells have larger cellular spread area, generate larger forces, and migrate faster. The functional differences were all predicted by a motor-clutch model for cell adhesion and migration where mesenchymal cells have an optimal level of CD44-mediated adhesion (clutches) relative to myosin motors, while proneural cells lack sufficient CD44 to match the myosin motor activity. Despite the faster migration, NRAS/Mesenchymal mice live longer, consistent with the presence of an anti-tumoral immune response that is lacking in PDGF/Proneural mice (Fig. 8D), dynamics that are readily captured computationally with little parameter adjustment using a 3-D Brownian dynamics tumor simulator (BDTS). Overall, this work establishes an integrated *in vivo* genetic and biophysical modeling framework to connect animal model and human transcriptionally-defined subtypes to fundamental mechanistic understanding, which has the potential to enable a new modeling-centric approach to clinical translation with application in a wide range of cancers (Brubaker and Lauffenburger, 2020).

MATERIALS AND METHODS:

Generation of mouse tumor models

All animal studies were conducted according to guidelines approved by the Institutional Animal Care and Use Committee at the University of Minnesota. All animals were housed in a daily monitored animal facility. FVB/NJ strain of mice were used in this study. Malignant gliomas were induced in neonatal mice by DNA plasmid injection into the right lateral ventricle as described previously (Calinescu et al., 2015; Wiesner et al., 2009). Briefly, neonatal mice were injected with 1 µg of plasmid DNA mixed with polyethyleneimine (jetPEI, Polyplus, Berkeley, CA), and 5% dextrose in a total volume of 2 µL at a rate of 0.7 µL/min. The following four plasmids were used (1:1:1:1) ratio: empty vector, pT2/C-Luc/PGK-SB100, pT/CMV-LgTAg-IRES-GFP, pT2/Cag-NrasV12 or pT2/Cag-mPDGF. Animals were monitored daily for morbidity by bioluminescent imaging.

Immunohistochemistry of mouse tumor sections

Formalin fixed and paraffin embedded (FFPE) mouse brain tissues were used to prepare 4 µm thick slides. FFPE tissue slides were stained with hematoxylin and eosin (H&E) or IHC using standard methods. Table S6 contains a list of antibodies and reagents used for antigen retrieval, blocking and detection.

Quantification of IHC staining of mouse tumor sections

Immunohistochemistry data was quantified by counting the number of pixels in an image that were positively DAB stained. To avoid user bias and subjective counting, k-means clustering was used to identify pixels representing areas of positive DAB, hematoxylin staining, and background. In this implementation, every pixel in an analyzed image is assigned to one of four clusters, each cluster representing a different component in the image: positive DAB-stained areas (brown), positive hematoxylin counter-stained areas (blue), unstained tissue (light blue), and background glass slide (beige). Digital images of equal sizes (2000x2000 pixels) of DAB stained and hematoxylin counterstained tumor samples were converted from RGB to the HSV color model.

Using a custom written MATLAB algorithm, user input is used to define areas representing the four components (positive DAB stain, hematoxylin counterstain, unstained tissue, and background glass slide). These points are used as the initial estimates for the centroid locations of each of the four clusters. The squared Euclidean distance between each pixel's HSV coordinates and the HSV coordinates of each cluster's centroid is computed. Each pixel is then assigned to the cluster with the minimum squared Euclidean distance to the cluster centroid. Cluster centroids are recalculated as the mean of the HSV coordinated of all current members. This process is iterated until the centroid of each cluster is stable. The number of pixels in the positive DAB-stained cluster is used to quantify percent positive pixels in Figure 7E-H.

Transcriptional profiling of mouse tumors

Mice were euthanized in a CO_2 chamber and perfused transcardially with isotonic saline. Mouse brains were extracted and GFP goggle (#FHS/EF-2G2; BLS-ltd, Budapest, Hungary) was used to dissect GFP-positive tumor tissues from NRAS and PDGF mouse brains. Two matched normal brain tissues were collected from brain regions away from the tumor and an additional normal brain tissue sample was collected from a health FVB adult mouse. All samples were immediately placed in *RNALater* solution (Sigma, St. Louis, MO) for 24 hours then flash frozen in liquid nitrogen and stored in -80 °C for downstream processing. RNA extraction and sequencing were performed at the University of Minnesota Genomics Center (UMGC, Minneapolis, MN). RNA was extracted using *RNAeasy* Plus Universal Mini kit (Qiagen, Venlo, Netherlands) and libraries were prepared using *TruSeq* stranded mRNA (Illumina, San Diego, CA).

Next-generation sequencing was performed on the prepared RNA libraries using an Illumina HiSeq 2500 device in high output mode and generated 51 bp reads with an approximate depth of 20 million paired reads per sample. Mapping and expression calculations were generated using the rnaseq-pipeline of Gopher-pipelines (https://bitbucket.org/jgarbe/gopher-pipelines), which executed TopHat2 (Kim et al., 2013) and Cuffnorm (Trapnell et al., 2010) using the UCSC mm10 version of the mouse reference genome. Fastq files and the Cuffnorm output were deposited at Gene Expression Omnibus (GSE161154).

Human GBM transcriptomic data

UNC RNASeqV2 level 3 expression (normalized RSEM) profiles of 171 samples (TCGA-GBM) were retrieved from Broad GDAC Firebrowse (Brennan et al., 2013). IDH status and subtype information were added to each sample based on the *Wang et al.* classification (Wang et al., 2017). For downstream analysis, 147 IDH-WT samples were used (57 Classical; 52 Mesenchymal; 38 Proneural).

Clustering analysis of mouse and human expression profiles

To analyze the transcriptional profiles of mouse and human datasets, a value of 0.1 was added to all FPKM and RSEM values to minimize the impact of inaccurate low values (Scott et al., 2018). The expression data was log transformed and mean centered and transcripts with Standard Deviation > 1 were clustered using average linkage hierarchical clustering in MATLAB. Pearson correlation was used as the similarity metric. A custom written MATLAB script was used to systematically identify transcriptional clusters within each dataset. In mouse dataset, a correlation greater than 0.5 and > 100 transcripts were used to identify gene clusters. Whereas, in human dataset, a correlation greater than 0.2 and >100 transcripts were used. Fisher's exact test was used to compare cluster memberships in Figure 1C. All genes identified within each cluster are listed in Table S2.

To quantify the relative expression of gene clusters in Figure 1D and subtype gene signature set in Figure S2C and S2D, the average relative expression of each gene set was computed for all samples. The average relative expression from each sample was plotted and used to calculate mean relative expression within each mouse cohort and within human GBM molecular subtype.

Generation of mouse primary tumor lines

For each line, a tumor bearing mouse was euthanized and transcardially perfused with isotonic saline. Tumor tissue was collected and minced with a scalpel. Minced tumor fragments were incubated with PBS for 15 min at 37 °C. Tumor fragments were further dissociated by mixing them up and down using a 1000 µl micropipette. Finally, tumor suspension was passed through a 40 µm sterile cell strainer (Thermo Fischer Scientific, Waltham, MA) and filtrate was spun down and plated on a Matrigel (354230; Corning, Corning, NY) coated T-75 flasks (Corning, Corning, NY) using NSC media which consisted of DMEM/F12 (Gibco 11320033; Thermo Fischer Scientific, Waltham, MA) with 1X B-27 supplement (Gibco 12587010, Thermo Fischer Scientific, Waltham, MA) and 1X penicillin/streptomycin (Corning, Corning, NY). Twenty ng/ml EGF (PeproTech, Rocky Hill, NJ) and FGF (PeproTech, Rocky Hill, NJ) were added to the cell culture media every 2-3 days. Cells were cultured in a 37 °C 5% CO_2 incubator. Once a confluent layer was achieved, cells were detached using 0.25% Trypsin EDTA (Corning, Corning, NY) and frozen down for later use.

Once tumor lines were established, cells were grown as neurospheres using NSC media and Ultra-Low Attachment 6-well plates (Corning, Corning, NY). Neurospheres were dissociated using accutase (Innovative Cell Technologies, San Diego, CA). In total, six different mouse primary tumor lines were established: three NRAS and three PDGF.

Patient-derived xenograft (PDX) cell line culture

The patient-derived xenograft (PDX) cell lines were taken from the Mayo Clinic GBM PDX collection (managed by Dr. Jann Sarkaria, Mayo Clinic, Rochester, MN). Three mesenchymal PDX lines (GBM 16, 39 and 44) and three proneural PDX lines (GBM 64, 80 and 85) were selected to study their migration in organotypic mouse brain slice. Cells were cultured on Matrigel (354230; Corning, Corning, NY) coated tissue culture flasks in a 37 °C 5% CO_2 incubator. NSC media was used to culture PDX cell lines and 20 ng/ml EGF and FGF were added to the cell culture media every 2-3 days.

Ex vivo confocal imaging of tumor-bearing brain slices

Tumor-bearing mice were sacrificed when bioluminescence signals were around 5×10^7 radiance (p/sec/cm^2/sr). Mice were euthanized in a CO_2 chamber and perfused transcardially with isotonic saline. Mouse brains were extracted and kept in chilled artificial cerebrospinal fluid (124 mM NaCl, 2.5 mM KCl, 2.0 mM $MgSO_4$,1.25 mM KH_2PO_4, 26 mM $NaHCO_3$, 10 mM glucose). Coronal brain slices of thickness 300 µm were prepared using a vibratome (Leica Biosystems, Buffalo Grove, IL). Only one slice was used for live-cell imaging. Isolectin GS-IB4 (Alexa Fluor 568 Conjugate; Molecular Probes, Eugene, OR) was used to label the vasculature.

Before imaging, the slice was washed and transferred into a No. 0 glass bottom 35 mm culture dish (P35G-0-20-C; MatTek, Ashland, MA). A tissue culture anchor (SHD 42-15; Warner Instruments, Hamden, CT) was placed on top of the slice to prevent movement during imaging. The slice was then imaged on a Zeiss LSM 7 Live swept-field laser confocal microscope (Zeiss, Oberkochen, Germany) at 15-minute intervals for

568 up to 20 hours in humidified 5% CO_2 air at 37 ºC. Images were collected with a 20x
569 objective lens (Plan-ApoChromat 20X, 0.8 NA, Zeiss, Oberkochen, Germany). The
570 number of Z stacks of several regions of interest was adjusted to ensure that the data
571 acquisition of one frame in the time series was completed under 15 minutes (10-20
572 planes with 10 µm z-step was typically used). Maximum intensity projections from
573 multiple Z stacks were used to generate 2D images for quantitative morphological and
574 trajectory analysis. Images were registered by an affine transformation using ImageJ
575 StackReg plug-in (École Polytechnique Fédérale De Lausanne) to account for stage
576 drift and tissue relaxation during time-lapse imaging.

577

578 **Live-cell imaging of tumor cells in organotypic brain-slice culture**

579 Healthy mouse brain slices were prepared using the same method as tumor-
580 bearing brain slices above. For experiments using GFP-positive mouse primary tumor
581 lines, neurospheres were dissociated using accutase (Innovative Cell Technologies,
582 San Diego, CA). The protocol of grafting cancer cells into the brain slice was described
583 in details in our previous publication (Liu et al., 2019). Briefly, after creating a single cell
584 suspension, 300,000 cells in 3 mL of media were plated onto the brain slice. The cells
585 were co-cultured with the brain slice for 4 hours at 37 °C and 5% CO_2 before imaging to
586 promote cell infiltration into the brain slice. Phenol-free NSC media +2% FBS (Gibco,
587 Thermo Fischer Scientific, Waltham, MA) was used. The slices (Isolectin GS-IB4
588 stained) were washed several times using cell culture media and transferred into a No.
589 0 glass bottom 6-well plate (P06G-0-20-F; MatTek, Ashland, MA). The slices were
590 imaged on a confocal microscope with a 10X objective lens (Plan-ApoChromat 10X,

591 0.45 NA, Zeiss, Oberkochen, Germany). Similar imaging protocol as mentioned above
592 was applied.

593 For PDX cells, 500,000 – 800,000 cells were stained using DiO membrane dye
594 (V22886; Thermo Fisher Scientific, Waltham, MA) for 5 minutes and then washed twice
595 before plating onto the brain slice inside a 35mm tissue culture dish. The grafting of the
596 cells to the brain slice was similar to the mouse primary cells described above. The
597 slices were imaged on a confocal microscope using a 20X objective lens (Plan-
598 ApoChromat 20X, 0.8 NA, Zeiss, Oberkochen, Germany). Similar imaging protocol was
599 applied.

600 For both mouse primary tumor cells and PDX cells, we also acquired the
601 maximum intensity projections from multiple Z stacks and performed image registration
602 for further analysis for cell migration and morphology. Images were registered by an
603 affine transformation using ImageJ StackReg plug-in (École Polytechnique Fédérale De
604 Lausanne) to account for stage drift and tissue relaxation during time-lapse imaging.
605

606 **Single cell tracking and morphology analysis**

607 Single cell migration was tracked as previously described using a custom-written
608 image segmentation algorithm in MATLAB (Bangasser et al., 2017; Klank et al., 2017).
609 Using cell centroid coordinates, the mean squared displacement (MSD) of the cell
610 trajectories over time was calculated using the time interval overlap method (Dickinson
611 and Tranquillo, 1993). To quantify the dispersion of cells, the MSD over time was used
612 to calculate the random motility coefficient μ according to the equation ($MSD(t)=4\mu t$;
613 assuming 2-D geometry). Using segmented cell regions, cell area and cell aspect ratio,

614 defined as the ratio between the major and minor axis length of a fitted ellipse, were
615 measured for each individual tracked cell. Distributions of random motility coefficients,
616 cell area and cell aspect ratio for the different conditions were compared using the
617 Kruskal-Wallis test, which is a non-parametric rank-based test.

618

619 **Bioluminescence imaging and analysis**

620 Animals were monitored for tumor development and progression using
621 noninvasive bioluminescence imaging. Oncogene-injected animals were injected
622 intraperitoneally with 100 µl of 28.5 mg/ml luciferin (GoldBio, St. Louis, MO) prior to
623 imaging. Mice were then anesthetized using 3% isofluorane and imaged on an IVIS50
624 or IVIS100 instrument (Xenogen, Alameda, CA). Images were acquired ten minutes
625 after injection with five minutes exposure time (Xenogen LivingImage Software,
626 Alameda, CA). To avoid saturation, exposure time was reduced appropriately in fully
627 grown tumors and accounted for in the analysis. BL images were processed using a
628 custom written MATLAB algorithm where background signal was subtracted and pixels
629 away from the tumor were set to zero. BL signal from each animal was then normalized
630 to the initial time point when tumor was first detected.

631

632 **Quantification of proliferation of mouse primary tumor line**

633 To measure proliferation rate, 200,000 cells from each line were plated into an
634 ultra-low adhesion 6-well plate and grown as neurospheres. Growth factors were added
635 every 2-3 days. At day six, neurospheres were dissociated and cells counted. After

636 counting, the remaining cells were replated and resumed growing as neurospheres.
637 Cells were also counted and replated at day nine and day 13. Experiment was repeated
638 three times using each of five mouse primary tumor lines (three NRAS and two PDGF
639 tumor lines). For each replicate, the average cell count for each cohort was calculated
640 using the cell count from the different corresponding tumor lines.

641

642 **Traction force measurements**

643 Traction force measurements of mouse primary tumor lines were performed
644 using traction force microscopy on polyacrylamide gels embedded with 0.2 µm crimson
645 fluorescent beads (Thermo Fischer Scientific, Waltham, MA) and coated with Type-I
646 Collagen (Corning, Corning, NY). Collagen coated polyacrylamide gels of varying
647 Young's modulus were prepared as previously described (Bangasser et al., 2017; Wang
648 and Pelham, 1998). Briefly, 0.7, 4.6, and 9.3 kPa polyacrylamide polymer mixture with
649 fluorescent beads were cast onto a No. 0 glass bottom dish then coated with Type-I
650 Collagen using Sulfo-SANPAH (Thermo Fischer Scientific, Waltham, MA). Mouse
651 primary tumor cells were dissociated from neurospheres and plated on prepared gels at
652 low density (1-5 cells/mm^2) using NSC media +2% FBS.

653 To measure force transmission, Traction Force Microscopy (TFM) was performed
654 as previously described (Bangasser et al., 2017). Briefly, Nikon TiE and Ti2
655 epifluorescence microscopes were used to image fluorescent bead positions before and
656 after cell detachment via trypsin. A Zyla 5.5 sCMOS camera (Andor Technology,
657 Belfast, United Kingdom) and a 40x/0.95NA Ph2 lens with 1.5x intermediate zoom (60x
658 total magnification, 110 nm spatial sampling) was used. Cells were maintained at 37 °C

and 5% CO_2 for the duration of imaging using an Oko lab Bold Line top stage humidified incubator (Okolab, Ottaviano, Italy). At each stage position, a phase contrast image of the cell was acquired. Next, an image of fluorescent beads at the top surface of the gel was captured using a 575/25 nm LED and eGFP/mCherry filter set with LED fluorescence illumination from a SpectraX Light Engine (Lumencor, Beaverton, OR). Media in dishes was carefully removed, cells were detached with 0.25% trypsin/EDTA (Corning, Corning, NY), and fluorescence images of beads in the absence of cells were acquired at saved stage positions.

Using a previously described method (Bangasser et al., 2017), the displacement field was determined using particle image velocimetry (PIV) using the before and after bead images. A window size of 80-pixels (8.8 μm) square was used in PIV and a final lattice spacing of 20 pixels (2.2 μm) was achieved. Stress and displacement vectors were obtained by solving the inverse Boussinesq problem in Fourier space (Butler et al., 2002). By integrating the product of the stress and displacement vectors over the entire image, substrate strain energy was determined as previously described (Bangasser et al., 2017).

Stochastic cell migration simulator

The previously described (Bangasser et al., 2017; Klank et al., 2017) cell migration simulator (CMS v1.0) was used to simulate cells migration dynamics in response to changes in cell adhesion. The parameters used in the simulations are presented in Table S3. The number of adhesive clutches (N_c) was adjusted to model the change in adhesion observed between PDGF/Proneural and NRAS/Mesenchymal tumors. N_c of

682 2500 and 7500 clutches were used to simulate PDGF/Proneural and
683 NRAS/Mesenchymal tumor cells, respectively. Four hours of cell dynamics were
684 simulated and the first hour was excluded from analysis to allow the system to reach
685 steady state. Analysis was performed using a ten-minute sampling interval as previously
686 described (Bangasser et al., 2017).

687

688 **Brownian dynamics tumor simulator (BDTS)**

689 The Brownian dynamics tumor simulator was used as previously described with
690 modifications (Klank et al., 2018; Ray et al., 2018). In the present study, we extended
691 the BTDS to 3-dimentional tumors and incorporated immune cells' dynamics as shown
692 schematically in Figure 8A. Briefly, simulations started with 27 cancer cells, modeled as
693 rigid sphere with radius (r_{cancer}), placed in a 3x3x3 grid where the distance between
694 each cancer cell (center-center) is $3*r_{cancer}$. In simulation including immune response,
695 eight T cells, also modeled as rigid sphere with radius (r_{CTL}), were included, and each
696 was placed $1.5*r_{cancer}$ away from a randomly selected cancer cell. At each simulation
697 time step of 1 min, cancer and T cells are allowed to move randomly and grow as
698 spheres with a linear volumetric growth rate. Movement and growth are rejected if the
699 newly assigned space is already occupied by a like cell (i.e. no-overlap enforced
700 between cancer cells and between T cells). However, a cancer cell and T cell contact
701 occurs when a proposed cell movement put the distance between cell centers less than
702 or equal ($r_{CTL}+r_{cancer}$). The duration of the contact is ($1/k_{dissoc}$), in this case 10 minutes.
703 For every contact, both cancer cell and T cell take a "hit" that reduces their hit points
704 (HP) by one. Both cancer cell and T cell have limited HP and once HP is depleted

(equals 0), the cell dies or become exhausted. For NRAS simulations, T cells were added to the tumor simulator and T cell-mediated killing was simulated. For PDGF simulation, only cancer cells were simulated. Cancer cell motility was estimated from *ex vivo* brain slice imaging of tumor cells (Figure 3C) and proliferation rate was estimated from the *in vitro* proliferation of mouse primary tumor lines (Figure 7D). The rest of parameters were estimated based on previous published work or used as an adjustable parameter (see Table S5).

Statistical analysis

Fisher's exact test was used to compare the mouse and human transcriptomic clusters. One-way analysis of variance was used to compare transcript levels. Analysis of covariance (ANCOVA) was used to compare between the two regression lines in Figure 5C. Rank test, Kruskal-Wallis, one-way analysis of variance was used to compare single cell behaviors and IHC quantifications. Where appropriate, a subsequent Dunn-Sidak test for multiple comparisons was performed.

DATA AND CODE AVAILABILITY:

All data and codes are available on the Odde laboratory website (oddelab.umn.edu) or on request from the corresponding author. Fastq files and the Cuffnorm output were deposited at Gene Expression Omnibus (GSE161154).

AUTHORS CONTRIBUTION:

GAS, BLK, BRT, SSR, DAL and DJO contributed to study initiation, conception and design.
GAS, CJL, BCB and DJO contributed to writing the manuscript
GAS, BCB and JMF contributed to developing mouse tumors
GAS, SKR and ALS contributed to the analysis of transcriptomic data.
GAS ran and analyzed the cell migration simulations
GAS and CJL contributed to the acquisition and analysis of glioma cell migration
GAS established tumor lines and performed traction force measurements
GAS, BCB and HBC contributed to imaging and analysis of histological sections
NG, PCR, DM and DJO contributed to the design and implementation of the Brownian Dynamics Tumor Simulator
All authors contributed to the revisions of the manuscript

CONFLICT OF INTEREST STATEMENTS:

DAL is the co-founder and co-owner of several biotechnology companies including NeoClone Biotechnologies, Inc., Discovery Genomics, Inc. (recently acquired by immusoft, Inc.), B-MoGen Biotechnologies, Inc. (recently acquired by Bio-Techne Corporation), and Luminary Therapeutics, Inc. DAL holds equity in, serves as a Senior Scientific Advisor for and Board of Director member for Recombinetics, a genome editing company. DAL consults for Genentech, Inc., which is funding some of his research. The business of all these companies is unrelated to the contents of this manuscript.

ACKNOWLEDGMENTS:

The authors would like to thank Drs. Chris Wilke and Clark C. Chen for helpful discussion. This work was supported by National Institutes of Health grant U54 CA210190 to SSR, DAL and DJO and U54CA210180 to JNS. DAL acknowledges the American Cancer Society Research Professor grant, the John and Jean Hedberg Brain Tumor Fund, and the Children's Cancer Research Fund. The authors acknowledge the Minnesota Supercomputing Institute (MSI) and University of Minnesota Genomic Center at the University of Minnesota for providing resources that contributed to the research results reported within this paper. We also acknowledge the Comparative Pathology, Cancer Bioinformatics, and Cytogenomics Shared Resources at the Masonic Cancer Center at the University of Minnesota for services.

REFERENCES:

Ahuja, D., Sáenz-Robles, M.T., and Pipas, J.M. (2005). SV40 large T antigen targets multiple cellular pathways to elicit cellular transformation. Oncogene *24*, 7729–7745.

Arima, Y., Hayashi, H., Kamata, K., Goto, T.M., Sasaki, M., Kuramochi, A., and Saya, H. (2010). Decreased expression of neurofibromin contributes to epithelial-mesenchymal transition in neurofibromatosis type 1. Exp. Dermatol. *19*.

Bangasser, B.L., Rosenfeld, S.S., and Odde, D.J. (2013). Determinants of maximal force transmission in a motor-clutch model of cell traction in a compliant microenvironment. Biophys. J. *105*, 581–592.

Bangasser, B.L., Shamsan, G.A., Chan, C.E., Opoku, K.N., Tüzel, E., Schlichtmann, B.W., Kasim, J.A., Fuller, B.J., McCullough, B.R., Rosenfeld, S.S., et al. (2017). Shifting the optimal stiffness for cell migration. Nat. Commun. *8*.

Bhat, K.P.L., Balasubramaniyan, V., Vaillant, B., Ezhilarasan, R., Hummelink, K., Hollingsworth, F., Wani, K., Heathcock, L., James, J.D., Goodman, L.D., et al. (2013). Mesenchymal Differentiation Mediated by NF-κB Promotes Radiation Resistance in Glioblastoma. Cancer Cell *24*, 331–346.

Bloushtain-Qimron, N., Yao, J., Snyder, E.L., Shipitsin, M., Campbell, L.L., Mani, S.A., Hu, M., Chen, H., Ustyansky, V., Antosiewicz, J.E., et al. (2008). Cell type-specific DNA methylation patterns in the human breast. Proc. Natl. Acad. Sci. U. S. A. *105*, 14076–14081.

Boissonnas, A., Fetler, L., Zeelenberg, I.S., Hugues, S., and Amigorena, S. (2007). In vivo imaging of cytotoxic T cell infiltration and elimination of a solid tumor. J. Exp. Med. *204*, 345–356.

Brennan, C.W., Verhaak, R.G.W., McKenna, A., Campos, B., Noushmehr, H., Salama, S.R., Zheng, S., Chakravarty, D., Sanborn, J.Z., Berman, S.H., et al. (2013). The somatic genomic landscape of glioblastoma. Cell *155*, 462.

Brubaker, D.K., and Lauffenburger, D.A. (2020). Translating preclinical models to humans. Science (80-.). *367*, 742–743.

Butler, J.P., Tolić-Nørrelykke, I.M., Fabry, B., and Fredberg, J.J. (2002). Traction fields, moments, and strain energy that cells exert on their surroundings. Am. J. Physiol. Cell Physiol. *282*, C595-605.

Calinescu, A.A., Núñez, F.J., Koschmann, C., Kolb, B.L., Lowenstein, P.R., and Castro, M.G. (2015). Transposon mediated integration of plasmid DNA into the subventricular zone of neonatal mice to generate novel models of glioblastoma. J. Vis. Exp. 52443.

Chaffer, C.L., and Weinberg, R.A. (2011). A perspective on cancer cell metastasis. Science (80-.). *331*, 1559–1564.

Chan, C.E., and Odde, D.J. (2008). Traction dynamics of filopodia on compliant substrates. Science *322*, 1687–1691.

Dickinson, R.B., and Tranquillo, R.T. (1993). Optimal estimation of cell movement

indices from the statistical analysis of cell tracking data. AIChE J. *39*, 1995–2010.

DiMilla, P.A., Barbee, K., and Lauffenburger, D.A. (1991). Mathematical model for the effects of adhesion and mechanics on cell migration speed. Biophys. J. *60*, 15–37.

Doucette, T., Rao, G., Rao, A., Shen, L., Aldape, K., Wei, J., Dziurzynski, K., Gilbert, M., and Heimberger, A.B. (2013). Immune heterogeneity of glioblastoma subtypes: extrapolation from the cancer genome atlas. Cancer Immunol. Res. *1*, 112–122.

Estabridis, H.M., Jana, A., Nain, A., and Odde, D.J. (2018). Cell Migration in 1D and 2D Nanofiber Microenvironments. Ann. Biomed. Eng. *46*, 392–403.

Fehon, R.G., McClatchey, A.I., and Bretscher, A. (2010). Organizing the cell cortex: The role of ERM proteins. Nat. Rev. Mol. Cell Biol. *11*, 276–287.

Freeman, S.A., Vega, A., Riedl, M., Collins, R.F., Ostrowski, P.P., Woods, E.C., Bertozzi, C.R., Tammi, M.I., Lidke, D.S., Johnson, P., et al. (2018). Transmembrane Pickets Connect Cyto- and Pericellular Skeletons Forming Barriers to Receptor Engagement. Cell *172*, 305-317.e10.

de Gooijer, M.C., Guillén Navarro, M., Bernards, R., Wurdinger, T., and van Tellingen, O. (2018). An Experimenter's Guide to Glioblastoma Invasion Pathways. Trends Mol. Med. *24*, 763–780.

Halle, S., Keyser, K.A., Stahl, F.R., Busche, A., Marquardt, A., Zheng, X., Galla, M., Heissmeyer, V., Heller, K., Boelter, J., et al. (2016). In Vivo Killing Capacity of Cytotoxic T Cells Is Limited and Involves Dynamic Interactions and T Cell Cooperativity. Immunity *44*, 233–245.

Halle, S., Halle, O., and Förster, R. (2017). Mechanisms and Dynamics of T Cell-Mediated Cytotoxicity In Vivo. Trends Immunol. *38*, 432–443.

Hanahan, D., and Weinberg, R.A. (2011). Hallmarks of cancer: The next generation. Cell *144*, 646–674.

Hara, T., Chanoch-Myers, R., Mathewson, N.D., Myskiw, C., Atta, L., Bussema, L., Eichhorn, S.W., Greenwald, A.C., Kinker, G.S., Rodman, C., et al. (2021). Interactions between cancer cells and immune cells drive transitions to mesenchymal-like states in glioblastoma. Cancer Cell.

Hoelzinger, D.B., Demuth, T., and Berens, M.E. (2007). Autocrine factors that sustain glioma invasion and paracrine biology in the brain microenvironment. J. Natl. Cancer Inst. *99*, 1583–1593.

Hou, J.C., Shamsan, G.A., Anderson, S.M., McMahon, M.M., Tyler, L.P., Castle, B.T., Heussner, R.K., Provenzano, P.P., Keefe, D.F., Barocas, V.H., et al. (2019). Modeling distributed forces within cell adhesions of varying size on continuous substrates. Cytoskeleton *76*, 571–585.

Janda, E., Lehmann, K., Killisch, I., Jechlinger, M., Herzig, M., Downward, J., Beug, H., and Grünert, S. (2002). Ras and TGFβ cooperatively regulate epithelial cell plasticity and metastasis: Dissection of Ras signaling pathways. J. Cell Biol. *156*, 299–313.

Kim, D., Pertea, G., Trapnell, C., Pimentel, H., Kelley, R., and Salzberg, S.L. (2013).

TopHat2: Accurate alignment of transcriptomes in the presence of insertions, deletions and gene fusions. Genome Biol. *14*, R36.

Klank, R.L., Decker Grunke, S.A., Bangasser, B.L., Forster, C.L., Price, M.A., Odde, T.J., SantaCruz, K.S., Rosenfeld, S.S., Canoll, P., Turley, E.A., et al. (2017). Biphasic Dependence of Glioma Survival and Cell Migration on CD44 Expression Level. Cell Rep. *18*, 23–31.

Klank, R.L., Rosenfeld, S.S., and Odde, D.J. (2018). A Brownian dynamics tumor progression simulator with application to glioblastoma. Converg. Sci. Phys. Oncol. *4*, 015001.

Koschmann, C., Calinescu, A.A., Nunez, F.J., Mackay, A., Fazal-Salom, J., Thomas, D., Mendez, F., Kamran, N., Dzaman, M., Mulpuri, L., et al. (2016). ATRX loss promotes tumor growth and impairs nonhomologous end joining DNA repair in glioma. Sci. Transl. Med. *8*.

Krusche, B., Ottone, C., Clements, M.P., Johnstone, E.R., Goetsch, K., Lieven, H., Mota, S.G., Singh, P., Khadayate, S., Ashraf, A., et al. (2016). EphrinB2 drives perivascular invasion and proliferation of glioblastoma stem-like cells. Elife *5*.

Kuleshov, M. V., Jones, M.R., Rouillard, A.D., Fernandez, N.F., Duan, Q., Wang, Z., Koplev, S., Jenkins, S.L., Jagodnik, K.M., Lachmann, A., et al. (2016). Enrichr: a comprehensive gene set enrichment analysis web server 2016 update. Nucleic Acids Res. *44*, W90–W97.

Lefranc, F., Brotchi, J., and Kiss, R. (2005). Possible future issues in the treatment of glioblastomas: special emphasis on cell migration and the resistance of migrating glioblastoma cells to apoptosis. J. Clin. Oncol. *23*, 2411–2422.

Legg, J.W., and Isacke, C.M. (1998). Identification and functional analysis of the ezrin-binding site in the hyaluronan receptor, CD44. Curr. Biol. *8*, 705–708.

Liu, C.J., Shamsan, G.A., Akkin, T., and Odde, D.J. (2019). Glioma Cell Migration Dynamics in Brain Tissue Assessed by Multimodal Optical Imaging. Biophys. J. *117*.

Mao, P., Joshi, K., Li, J., Kim, S.H., Li, P., Santana-Santos, L., Luthra, S., Chandran, U.R., Benos, P. V., Smith, L., et al. (2013). Mesenchymal glioma stem cells are maintained by activated glycolytic metabolism involving aldehyde dehydrogenase 1A3. Proc. Natl. Acad. Sci. U. S. A. *110*, 8644–8649.

McLendon, R., Friedman, A., Bigner, D., Van Meir, E.G., Brat, D.J., Mastrogianakis, G.M., Olson, J.J., Mikkelsen, T., Lehman, N., Aldape, K., et al. (2008). Comprehensive genomic characterization defines human glioblastoma genes and core pathways. Nature *455*, 1061–1068.

Mekhdjian, A.H., Kai, F., Rubashkin, M.G., Prahl, L.S., Przybyla, L.M., McGregor, A.L., Bell, E.S., Barnes, J.M., DuFort, C.C., Ou, G., et al. (2017). Integrin-mediated traction force enhances paxillin molecular associations and adhesion dynamics that increase the invasiveness of tumor cells into a three-dimensional extracellular matrix. Mol. Biol. Cell *28*, 1467–1488.

Menke-van der Houven van Oordt, C.W., Gomez-Roca, C., van Herpen, C., Coveler,

A.L., Mahalingam, D., Verheul, H.M.W., van der Graaf, W.T.A., Christen, R., Rüttinger, D., Weigand, S., et al. (2016). First-in-human phase I clinical trial of RG7356, an anti-CD44 humanized antibody, in patients with advanced, CD44-expressing solid tumors. Oncotarget *7*, 80046–80058.

Mooney, K.L., Choy, W., Sidhu, S., Pelargos, P., Bui, T.T., Voth, B., Barnette, N., and Yang, I. (2016). The role of CD44 in glioblastoma multiforme. J. Clin. Neurosci. *34*, 1–5.

Naor, D., Nedvetzki, S., Golan, I., Melnik, L., and Faitelson, Y. (2002). CD44 in cancer. Crit. Rev. Clin. Lab. Sci. *39*, 527–579.

Neftel, C., Laffy, J., Filbin, M.G., Hara, T., Shore, M.E., Rahme, G.J., Richman, A.R., Silverbush, D., Shaw, M.L., Hebert, C.M., et al. (2019). An Integrative Model of Cellular States, Plasticity, and Genetics for Glioblastoma. Cell *178*, 835-849.e21.

Núñez, F.J., Mendez, F.M., Kadiyala, P., Alghamri, M.S., Savelieff, M.G., Garcia-Fabiani, M.B., Haase, S., Koschmann, C., Calinescu, A.A., Kamran, N., et al. (2019). IDH1-R132H acts as a tumor suppressor in glioma via epigenetic up-regulation of the DNA damage response. Sci. Transl. Med. *11*.

Ozawa, T., Riester, M., Cheng, Y.K., Huse, J.T., Squatrito, M., Helmy, K., Charles, N., Michor, F., and Holland, E.C. (2014). Most human non-GCIMP glioblastoma subtypes evolve from a common proneural-like precursor glioma. Cancer Cell *26*, 288–300.

Patel, A.P., Tirosh, I., Trombetta, J.J., Shalek, A.K., Gillespie, S.M., Wakimoto, H., Cahill, D.P., Nahed, B. V., Curry, W.T., Martuza, R.L., et al. (2014). Single-cell RNA-seq highlights intratumoral heterogeneity in primary glioblastoma. Science (80-.). *344*, 1396–1401.

Phillips, H.S., Kharbanda, S., Chen, R., Forrest, W.F., Soriano, R.H., Wu, T.D., Misra, A., Nigro, J.M., Colman, H., Soroceanu, L., et al. (2006). Molecular subclasses of high-grade glioma predict prognosis, delineate a pattern of disease progression, and resemble stages in neurogenesis. Cancer Cell *9*, 157–173.

Pietras, A., Katz, A.M., Ekström, E.J., Wee, B., Halliday, J.J., Pitter, K.L., Werbeck, J.L., Amankulor, N.M., Huse, J.T., and Holland, E.C. (2014). Osteopontin-CD44 signaling in the glioma perivascular niche enhances cancer stem cell phenotypes and promotes aggressive tumor growth. Cell Stem Cell *14*, 357–369.

Polyak, K., and Weinberg, R.A. (2009). Transitions between epithelial and mesenchymal states: Acquisition of malignant and stem cell traits. Nat. Rev. Cancer *9*, 265–273.

Ponta, H., Sherman, L., and Herrlich, P.A. (2003). CD44: From adhesion molecules to signalling regulators. Nat. Rev. Mol. Cell Biol. *4*, 33–45.

Prahl, L.S., Bangasser, P.F., Stopfer, L.E., Hemmat, M., White, F.M., Rosenfeld, S.S., and Odde, D.J. (2018). Microtubule-Based Control of Motor-Clutch System Mechanics in Glioma Cell Migration. Cell Rep. *25*, 2591-2604.e8.

Prahl, L.S., Stanslaski, M.R., Vargas, P., Piel, M., and Odde, D.J. (2020). Predicting Confined 1D Cell Migration from Parameters Calibrated to a 2D Motor-Clutch Model. Biophys. J. *118*, 1709–1720.

924 Ray, A., Morford, R.K., Ghaderi, N., Odde, D.J., and Provenzano, P.P. (2018).
925 Dynamics of 3D carcinoma cell invasion into aligned collagen. Integr. Biol. (United
926 Kingdom) *10*, 100–112.

927 Riggs, T., Walts, A., Perry, N., Bickle, L., Lynch, J.N., Myers, A., Flynn, J., Linderman,
928 J.J., Miller, M.J., and Kirschner, D.E. (2008). A comparison of random vs. chemotaxis-
929 driven contacts of T cells with dendritic cells during repertoire scanning. J. Theor. Biol.
930 *250*, 732–751.

931 Scott, M.C., Temiz, N.A., Sarver, A.E., LaRue, R.S., Rathe, S.K., Varshney, J., Wolf,
932 N.K., Moriarity, B.S., O'Brien, T.D., Spector, L.G., et al. (2018). Comparative
933 transcriptome analysis quantifies immune cell transcript levels, metastatic progression,
934 and survival in osteosarcoma. Cancer Res. *78*, 326–337.

935 Stupp, R., Hegi, M.E., Gorlia, T., Erridge, S.C., Perry, J., Hong, Y.K., Aldape, K.D.,
936 Lhermitte, B., Pietsch, T., Grujicic, D., et al. (2014). Cilengitide combined with standard
937 treatment for patients with newly diagnosed glioblastoma with methylated MGMT
938 promoter (CENTRIC EORTC 26071-22072 study): a multicentre, randomised, open-
939 label, phase 3 trial. Lancet. Oncol. *15*, 1100–1108.

940 Toole, B.P. (2009). Hyaluronan-CD44 interactions in cancer: Paradoxes and
941 possibilities. Clin. Cancer Res. *15*, 7462–7468.

942 Trapnell, C., Williams, B.A., Pertea, G., Mortazavi, A., Kwan, G., Van Baren, M.J.,
943 Salzberg, S.L., Wold, B.J., and Pachter, L. (2010). Transcript assembly and
944 quantification by RNA-Seq reveals unannotated transcripts and isoform switching during
945 cell differentiation. Nat. Biotechnol. *28*, 511–515.

946 Tsukita, S., Oishi, K., Sato, N., Sagara, J., and Kawai, A. (1994). ERM family members
947 as molecular linkers between the cell surface glycoprotein CD44 and actin-based
948 cytoskeletons. J. Cell Biol. *126*, 391–401.

949 Verhaak, R.G.W., Hoadley, K.A., Purdom, E., Wang, V., Qi, Y., Wilkerson, M.D., Miller,
950 C.R., Ding, L., Golub, T., Mesirov, J.P., et al. (2010). Integrated genomic analysis
951 identifies clinically relevant subtypes of glioblastoma characterized by abnormalities in
952 PDGFRA, IDH1, EGFR, and NF1. Cancer Cell *17*, 98–110.

953 Vey, N., Delaunay, J., Martinelli, G., Fiedler, W., Raffoux, E., Prebet, T., Gomez-Roca,
954 C., Papayannidis, C., Kebenko, M., Paschka, P., et al. (2016). Phase I clinical study of
955 RG7356, an anti-CD44 humanized antibody, in patients with acute myeloid leukemia.
956 Oncotarget *7*, 32532–32542.

957 Wang, Y.-L., and Pelham, R.J. (1998). Preparation of a flexible, porous polyacrylamide
958 substrate for mechanical studies of cultured cells. Methods Enzymol. *298*, 489–496.

959 Wang, L.B., Karpova, A., Gritsenko, M.A., Kyle, J.E., Cao, S., Li, Y., Rykunov, D.,
960 Colaprico, A., Rothstein, J.H., Hong, R., et al. (2021). Proteogenomic and metabolomic
961 characterization of human glioblastoma. Cancer Cell *39*, 509-528.e20.

962 Wang, Q., Hu, B., Hu, X., Kim, H., Squatrito, M., Scarpace, L., deCarvalho, A.C., Lyu,
963 S., Li, P., Li, Y., et al. (2017). Tumor Evolution of Glioma-Intrinsic Gene Expression
964 Subtypes Associates with Immunological Changes in the Microenvironment. Cancer
965 Cell *32*, 42-56.e6.

966 Wiesner, S.M., Decker, S.A., Larson, J.D., Ericson, K., Forster, C., Gallardo, J.L., Long,
967 C., Demorest, Z.L., Zamora, E.A., Low, W.C., et al. (2009). De novo induction of
968 genetically engineered brain tumors in mice using plasmid DNA. Cancer Res. *69*, 431–
969 439.

970 Yonemura, S. (1998). Ezrin/Radixin/Moesin (ERM) Proteins Bind to a Positively
971 Charged Amino Acid Cluster in the Juxta-Membrane Cytoplasmic Domain of CD44,
972 CD43, and ICAM-2. J. Cell Biol. *140*, 885–895.

973 Yoshida, T., Matsuda, Y., Naito, Z., and Ishiwata, T. (2012). CD44 in human glioma
974 correlates with histopathological grade and cell migration. Pathol. Int. *62*, 463–470.

975

976

FIGURE LEGENDS:

Figure 1. *De novo* induced GBM mouse models using immune competent mice recapitulate mesenchymal and proneural subtypes of human GBM.
A) Schematic of mouse models. Plasmids encoding oncogenic drivers $NRAS^{G12V}$ or PDGFβ in combination with SV40LgTA were injected into P1 FVB mice to induce mesenchymal and proneural high grade gliomas, respectively. B) H&E and Ki67 IHC staining of NRAS and PDGF tumor sections. Scale bar: 50 μm. C) Unsupervised hierarchical clustering of mRNA expression in induced mouse tumors and human IDH-WT GBM-TCGA. Arrows indicate conserved genes present in both mouse and human gene clusters as defined by systematic comparison of gene cluster membership between datasets. D) Quantification of relative expression of mouse gene clusters within the mouse dataset (top panel) and human GBM molecular subtypes (lower panel). E,F) Relative expression of key mesenchymal and proneural genes within mouse tumors (E) and human tumors (F). Solid and dashed lines represent mean and median values, respectively. Error bar represents S.E.M. + p <0.05, * p <0.01, ** p<0.001, *** p<0.0001, **** p<0.00001.

Figure 2. Simulations of cell migration as a function of subtype based on CD44-mediated cellular adhesive clutches.
A) Schematic of proneural (low CD44) and mesenchymal (medium CD44, i.e. optimal) subtypes. B) Wind-rose plots of simulated cell trajectories on different stiffnesses (κ_{sub}= 0.1, 1, 10 pN/nm). C) Simulated cell migration random motility coefficients show higher migration with increased (optimal) adhesion across a range of substrate stiffnesses. D) Cell summed traction force exhibits higher traction forces with increased (optimal) adhesion across all stiffnesses. E, F) Cell spread area and aspect ratio increase with increased adhesion on substrate stiffnesses of 0.1 and 1 pN/nm. Error bars are S.E.M.

Figure 3. NRAS/Mesenchymal cells migrate faster, are more spread, and are more polarized than PDGF/Proneural cells in *ex vivo* tumor-bearing brain tissue. A) Representative *ex vivo* fluorescent montage of GFP-tagged tumor cells (green) and blood vessels staining using isolectin B4 (magenta). B) Wind rose plots of NRAS/Mesenchymal and PDGF/Proneural migrating tumor cell migration trajectories (N=46). C) NRAS/Mesenchymal cancer cell motility is faster than for PDGF/proneural cancer cells. D&E) NRAS/Mesenchymal cancer cells are more spread and polarized than PDGF/Proneural cells as evidenced by larger spread area and aspect ratio. Solid and dashed lines represent mean and median, respectively. N represents the number of individual cells tracked from 3 mice from each cohort. Error bars are S.E.M. +p <0.05, * p <0.01, ** p<0.001, *** p<0.0001, **** p<0.00001.

Figure 4. Cancer cell migration is subtype specific and independent of the tumor microenvironment and species.
A) Six representative images of primary isolated cells from each of the two mouse tumor subtypes (3 NRAS and 3 PDGF). GFP-tagged tumor cells (green) and blood vessels staining using isolectin B4 (magenta). B) NRAS/Mesenchymal primary isolated tumor cancer cells migrate faster than PDGF/Proneural primary isolated cancer cells in normal

mouse brain tissue as measured by random motility coefficient, see Video S2. C&D) Quantification of cell spread area and cell aspect ratio showing that NRAS/Mesenchymal cancer cells are more spread (C) and tend to be somewhat more polarized (D), p=0.075, than PDGF/Proneural cancer cells in healthy brain slices. E) Six representative images of proneural and mesenchymal PDX lines cells in healthy mouse brain tissue. Labeled tumor cells using DiO membrane dye (green) and blood vessel staining using isolectin B4 (magenta). F) Mesenchymal PDX cells migrate faster than proneural PDX cells in normal mouse brain tissue as measured by random motility coefficient, see Video S3. G&H) Quantification of cell spread area and cell aspect ratio showing that mesenchymal PDX cells are more spread (G) and are more polarized (H) than proneural PDX cells in healthy brain slices. Solid and dashed lines represent mean and median values respectively. N represents the number of individual cells tracked from 3 mouse primary cell lines from each cohort. Error bars are S.E.M. +p <0.05, * p <0.01, ** p<0.001, *** p<0.0001, **** p<0.00001.

Figure 5. NRAS/Mesenchymal cancer cells generate larger traction forces *in vitro* on 2D hydrogels and *ex vivo* in brain slices than PDGF/Proneural cancer cells. A) Representative phase contrast images and traction force magnitude heatmaps on type I collagen-coated polyacrylamide hydrogels across different substrate stiffnesses. B) NRAS/Mesenchymal cancer cells (red) generate higher traction forces as measured by total strain energy relative to PDGF/Proneural (blue) cancer cells. Measurement noise is presented (grey) across all stiffnesses. C) Similar to mouse brain slices, NRAS/Mesenchymal cancer cells (red) cultured on collagen-coated polyacrylamide hydrogels have larger spread area than PDGF cancer cells (blue). D &E) Tissue deformation visualized using temporal-color coding using 2 hours time-lapse and 15 minutes time interval. Mesenchymal PDX cells generate larger deformations of mouse brain capillaries (E) than proneural PDX cells shown in (D). Scale bar = 20 μm, and inset scale bar = 10 μm. Solid and dashed lines represent mean and median values, respectively. N represents individual cell measurements from three mouse primary cell lines from each cohort with a minimum of two technical replicates. Error bars are S.E.M. +p <0.05, * p <0.01, ** p<0.001, *** p<0.0001, **** p<0.00001.

Figure 6. NRAS/Mesenchymal mice live longer than PDGF/Proneural mice. A) Kaplan-Meier plot of animal survival for NRAS/Mesenchymal and PDGF/Proneural tumor-bearing mice shows extended survival of the NRAS/Mesenchymal cohort. Log rank Mantel–Cox test p<0.00001. B) Bioluminescence imaging (BLI) of NRAS/Mesenchymal mice shows slower growing tumors relative to PDGF/Proneural mice. C) Quantification of BLI integrated intensity for the two cohorts. Normalized BLI intensity for all data points and linear fits for each cohort. PDGF/Proneural slope=0.127±0.01191 and NRAS/Mesenchymal slope=0.0716±0.00343, D) Normalized cell count of primary isolated mouse tumor cells showing no significant difference in proliferation rate *in vitro* using neurosphere culture. Solid and dashed lines represent mean and median values, respectively. Error bars are S.E.M. +p <0.05, * p <0.01, ** p<0.001, *** p<0.0001, **** p<0.00001.

Figure 7. NRAS/Mesenchymal tumors are relatively immunologically "hot" and PDGF/Proneural tumors are immunologically "cold," consistent with human GBM subtypes. A, B) Clustering analysis of immune activators and suppressors previously reported in human GBM (Doucette *et al*., 2013). Similar to mesenchymal GBM, NRAS/Mesenchymal tumors have elevated immune activator and suppressor expression relative to normal brain tissue and PDGF/Proneural tumors. C) Expression of immune cell surface marker genes in mouse (top) and human (bottom) tumors shows elevated expression in NRAS/Mesenchymal tumors and human mesenchymal GBM tumors relative to PDGF/Proneural and human proneural GBM tumors. D) Immunohistochemistry (IHC) confirms elevated immune cell infiltration in NRAS tumors and associated elevation of immune-mediated killing of tumor cells. E,F,G,H) Quantification of IHC images using a k-means clustering algorithm. Solid and dashed lines represent mean and median values, respectively. Error bars are S.E.M. +p <0.05 * p <0.01, ** p<0.001, *** p<0.0001, **** p<0.00001.

Figure 8. Brownian dynamics tumor simulator (BDTS) of 3D NRAS/Mesenchymal and PDGF/Proneural tumors. A) Schematic showing a diagram of the model. B) Simulator output at day 0 and day 16 for PDGF and NRAS simulations. In NRAS simulations, dead cancer cells are larger grey spheres and T cells are smaller black spheres, see Video S4. C) Cancer cell count over time showing the difference in tumor growth in the presence of T cells with simulated PDGF/Proneural tumors growing faster than NRAS/mesenchymal tumors. D) Cartoon summary of the main findings depicting the relationship between molecular subtypes, cellular adhesion, cell migration, and immune response.

SUPPLEMENTARY FIGURE AND TABLES LEGENDS:

Figure S1. Unsupervised clustering of mouse tumor and healthy brain tissue transcriptomic profiles and pathway enrichment analysis. A) Heatmap showing expression profile of NRAS and PDGF tumors and healthy mouse brain tissues. Heatmap shows existence of three gene clusters: Tumor-specific cluster, normal brain tissue specific cluster and NRAS tumor-specific cluster. B,C&D) Gene ontology analysis of gene clusters was performed using EnrichR.

Figure S2. Clustering analysis of mouse and human tumors using gene signatures associated with classical, mesenchymal, and proneural subtypes. A) Heatmap shows the clustering of human GBM samples using subtype-specific gene signatures. B) Heatmap shows the clustering of mouse tumors using subtype-specific gene signatures. C&D) Quantification of subtype gene signatures within human GBM subtypes and NRAS and PDGF mouse tumors. Solid and dashed lines represent mean and median values respectively. Error bars are S.E.M. +p <0.05, * p <0.01, ** p<0.001, *** p<0.0001, **** p<0.00001.

Figure S3. Differential expression analysis of cell migration genes. Volcano plot depicting $-\log_{10}$(adj p value) calculated using FDR adjusted Student's t test versus $\log_2$(average FC) for individual genes in A) mouse tumors and B) human TCGA-GBM

Figure S4. Quantification of single cell migration and cell morphology. A, B, & C) *Ex vivo* migration and morphology data from each individual animal. D, E, & F) Migration and morphology data for each individual mouse primary tumor line in mouse organotypic brain slice. G, H, & I) Migration and morphology data for each individual PDX line in mouse organotypic brain slice.

Figure S5. BL image sequences showing tumor regression in some rare cases. All three surviving mice in NRAS cohort showed tumor regression.

Figure S6. Expression of immune checkpoint genes within mouse tumors. Expression of immune checkpoint genes were upregulated in NRAS tumors relative to PDGF tumors (B) similar to human mesenchymal and proneural (A).

Video S1. Related to Figure 3. GFP-positive NRAS and PDGF tumor cells migrating in tumor bearing brain slices over 10 hours. Green shows tumor cells and magenta shows blood vasculature. Scale bar: 100 µm.

Video S2. Related to Figure 4A. GFP-positive NRAS and PDGF primary tumor cells migrating in mouse organotypic brain slice over 16 hours. Green shows tumor cells and magenta shows blood vasculature. Scale bar: 100 µm.

Video S3. Related to Figure 4D. Proneural and mesenchymal human PDX GBM cells migrating in mouse organotypic brain slice over 16 hours. Green shows tumor cells

stained using green DiO membrane dye and magenta shows blood vasculature. Scale bar: 100 µm.

Video S4. Related to Figure 8. Brownian dynamics tumor simulator output showing simulated tumor growth.

Table S1. Related to Figure 1. FPKM expression of mouse tumors and healthy brain tissues.

Table S2. Related to Figure 1C. List of genes identified in each cluster (MC1, MC2, MC3, HC1, HC2, HC4).

Table S3. Related to Figure 2. List of cell migration simulator parameter values.

Table S4. Related to Figure 4. Characteristics of patient-derived xenograft (PDX) lines used in this study.

Table S5. Related to Figure 8. List of Brownian dynamics tumor simulator parameter values.

Table S6. List of antibodies and reagents used in IHC staining.

1158 **Table S3:** Cell migration simulator parameter values

Symbol	Parameter	Value
N_m	Total number of motors	10,000
N_c	Total number of clutches	250; 750
A_{tot}	Total possible actin protrusion length	100 μm
v_p*	Maximum actin polymerization velocity	200 nm/s
k_{mod}*	Maximum module birth rate	1 s^{-1}
k_{cap}	Module capping rate	0.001 s^{-1}
l_{in}	Initial module length	5 μm
l_{min}	Minimum module length	0.1 μm
κ_{cell}	Cell spring constant	10,000 pN/nm
$n_{c,cell}$	Number of cell body clutches	10;
n_m*	Maximum number of module motors	0.1*N_c
F_m	Motor stall force	2 pN
v_m*	Unloaded motor velocity	120 nm/s
n_c*	Maximum number of module clutches	75; 750
k_{on}	Clutch on-rate	1 s^{-1}
k_{off}*	Clutch unloaded off-rate	0.1 s^{-1}
κ_c	Clutch spring constant	0.8 pN/nm
F_b	Characteristic clutch rupture force	2 pN
κ_s	Substrate spring constant	Variable

1159

1160 **Table S4:** Characteristics of patient-derived xenograft (PDX) lines used in this study

GBM	Xenograft start	Sex	Molecular subtype (RNAseq)
GBM16	2002	F	mesenchymal
GBM39	2003	M	mesenchymal
GBM44	2003	F	mesenchymal
GBM64	2006	F	proneural
GBM80	2007	M	proneural
GBM85	2008	M	proneural

1161

Table S5: Brownian dynamics tumor simulator parameters values

Parameter Name	Parameter	Value	Units	Reference
Cancer cell radius	r_{cancer}	10	μm	
T cell radius	r_{CTL}	3	μm	
Cancer cell motility	D_{cancer}	7.8; 42	$\mu m^2/h$	This study
T cell motility	D_{CTL}	300	$\mu m^2/hr$	(Boissonnas et al., 2007; Halle et al., 2016)
Cancer cell proliferation	p_{cancer}	0.5	1/d	This study
T cell proliferation	p_{CTL}	1	1/d	(Riggs et al., 2018)
Contact duration	$1/k_{dissoc}$	10	min	(Halle et al., 2016, 2017)
Cancer cell HP*	HP_{cancer}	1	contacts	(Halle et al., 2016)
T cell HP*	HP_{CTL}	20	contacts	Unknown, adjustable

1184 **Table S6:** IHC antibodies and reagents used in Figure 1A and Figure 7D

IHC	Antibody	Antigen retrieval	Blocking	Detection
Ki67	CRM325	High pH EDTA	Dako protein block	Dako rabbit envision
CD3a	A0452	High pH EDTA	Dako protein block	Biocare rat detection
IBA-1	AB107159	Low pH citrate	Dako protein block	Biocare goat detection
Cleaved Caspase-3	Asp175	High pH EDTA	Dako protein block	Dako rabbit envision
Granzyme B	D6E9W	Low pH citrate	Vectastain, goat serum	Vectastain ABC-HRP

1185

Figure 1

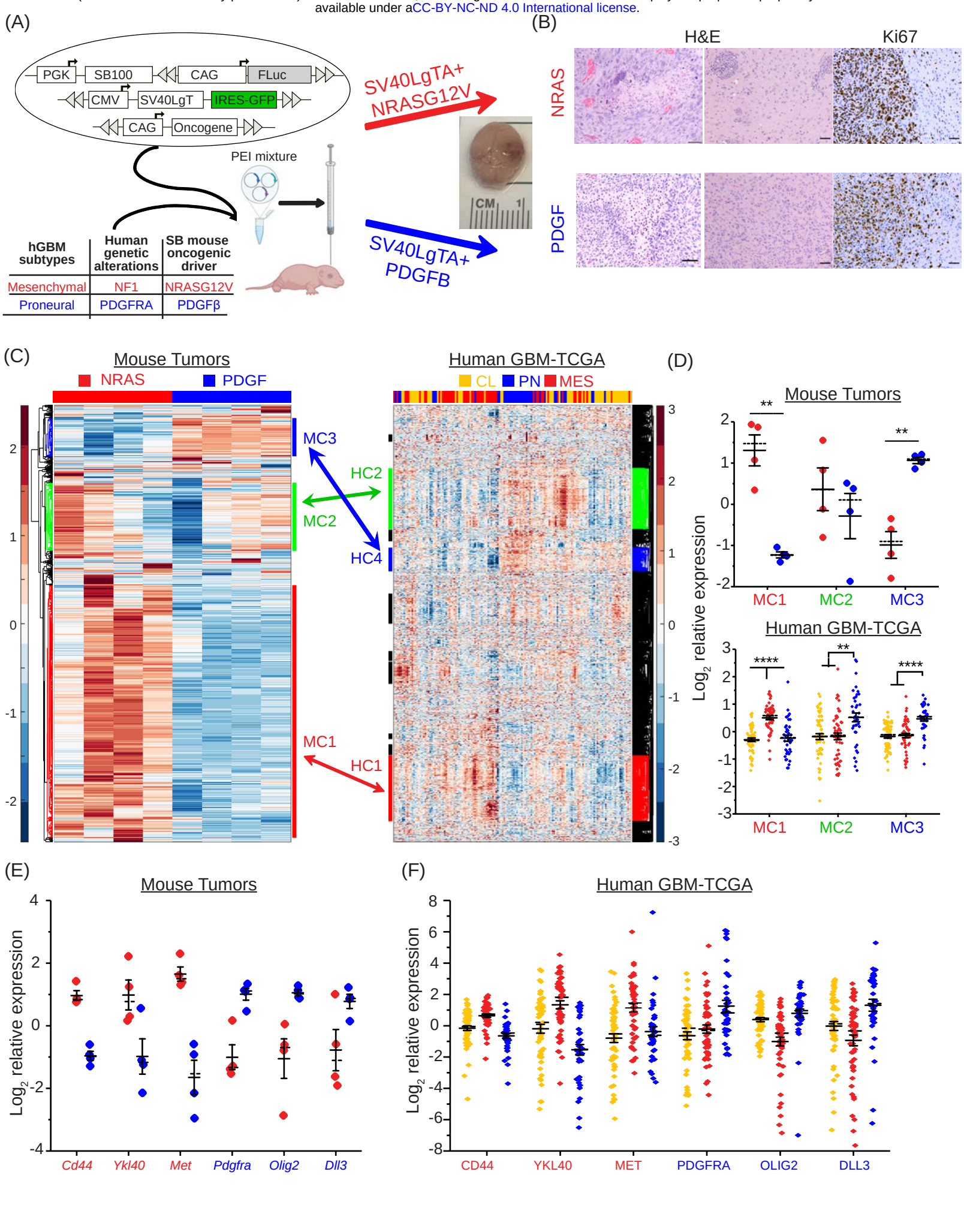

Figure 2

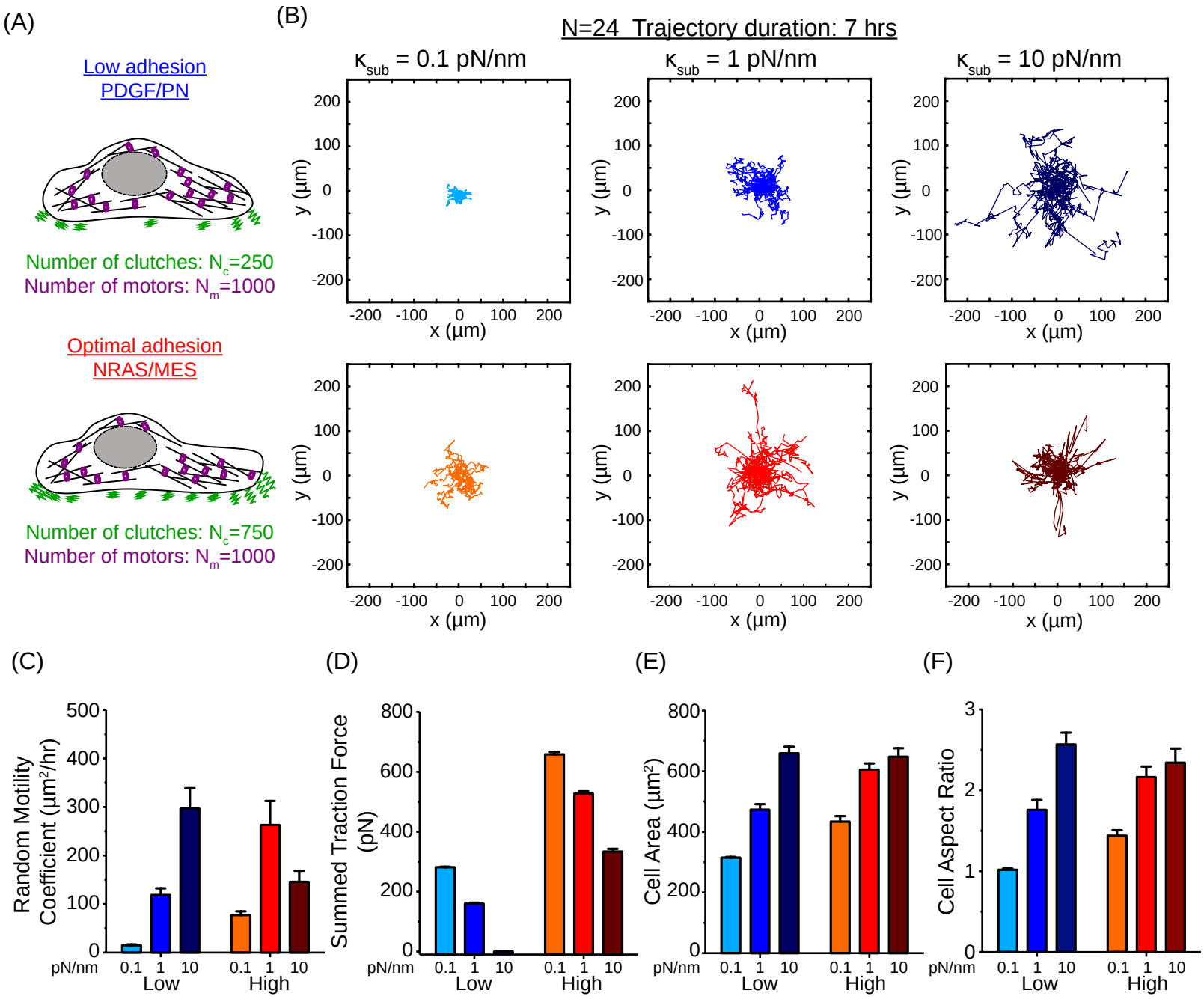

Figure 3

(A)

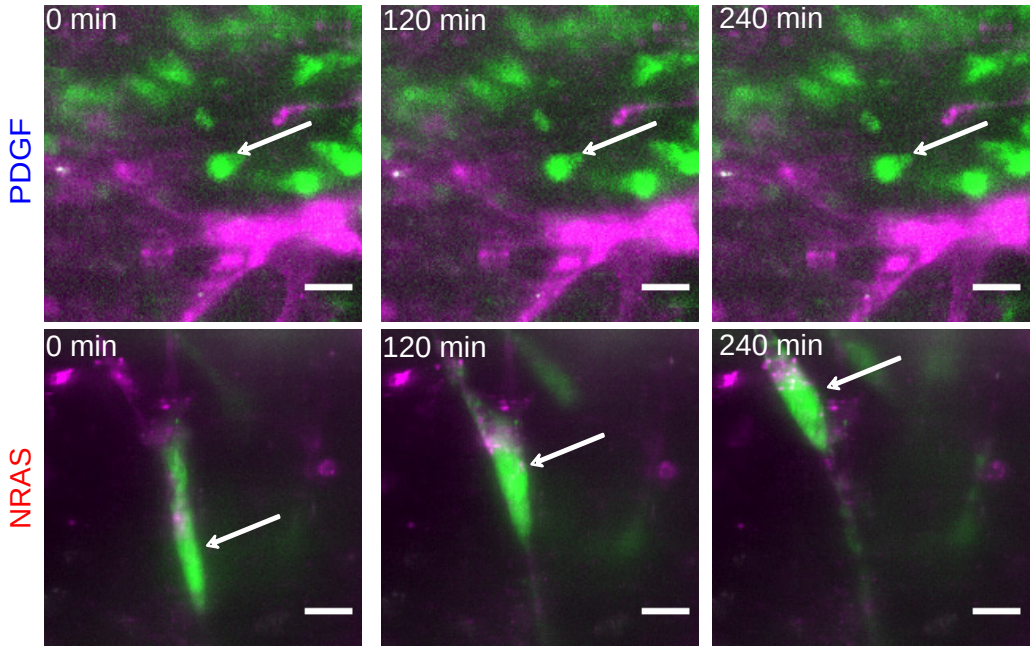

(B)

N=46: trajectory duration 3hrs

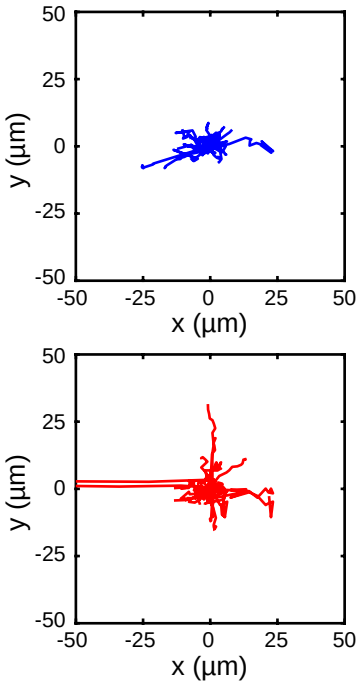

(C)

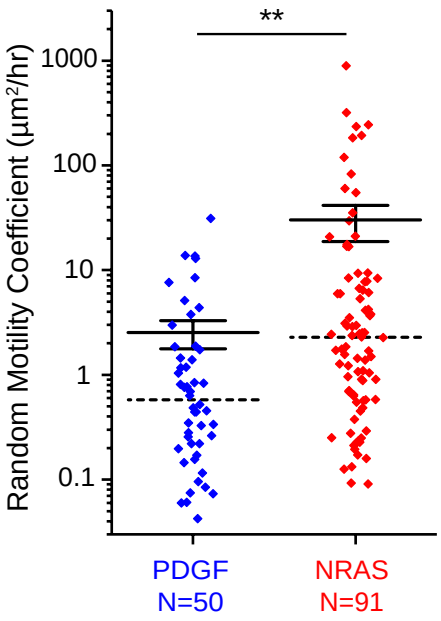

(D)

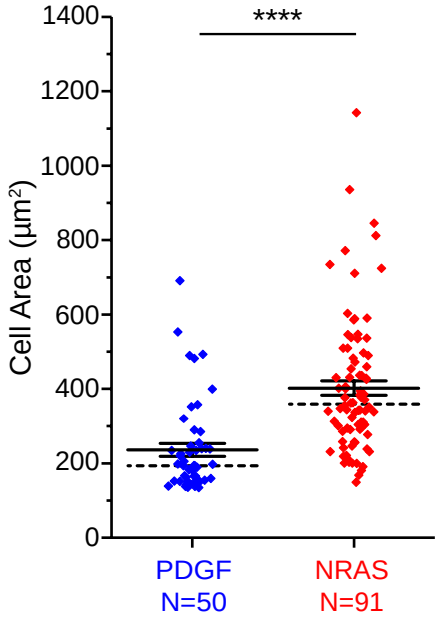

(E)

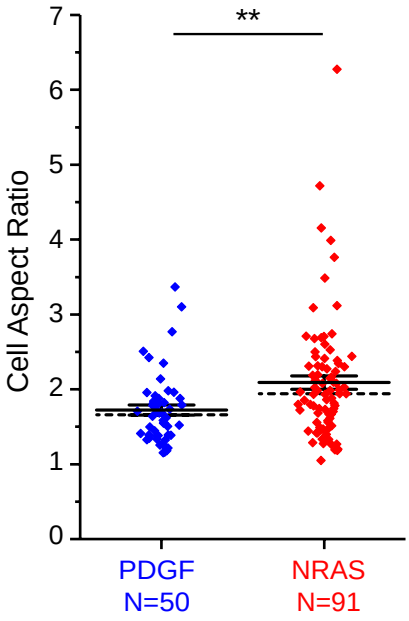

Figure 4

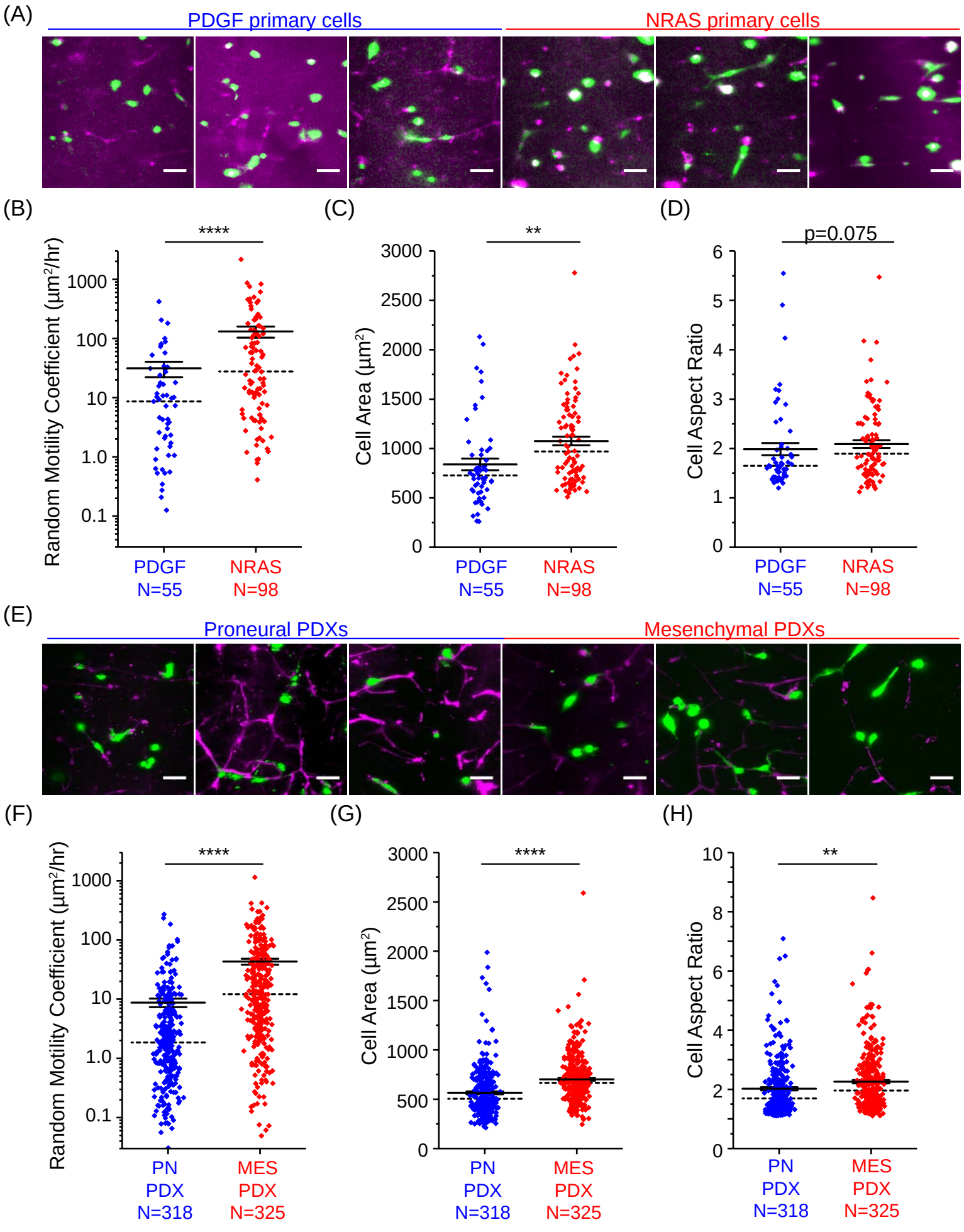

Figure 5

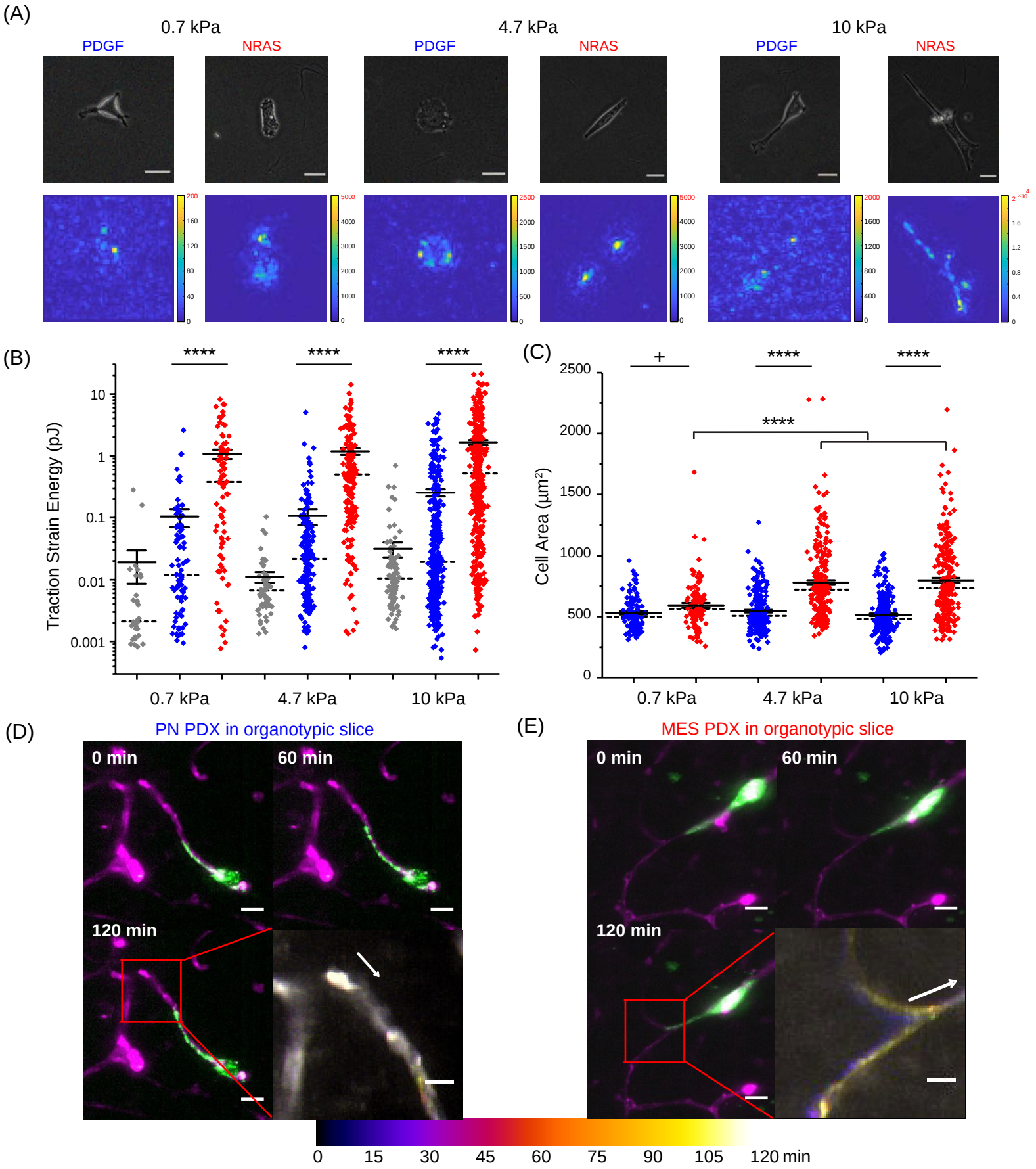

Figure 6

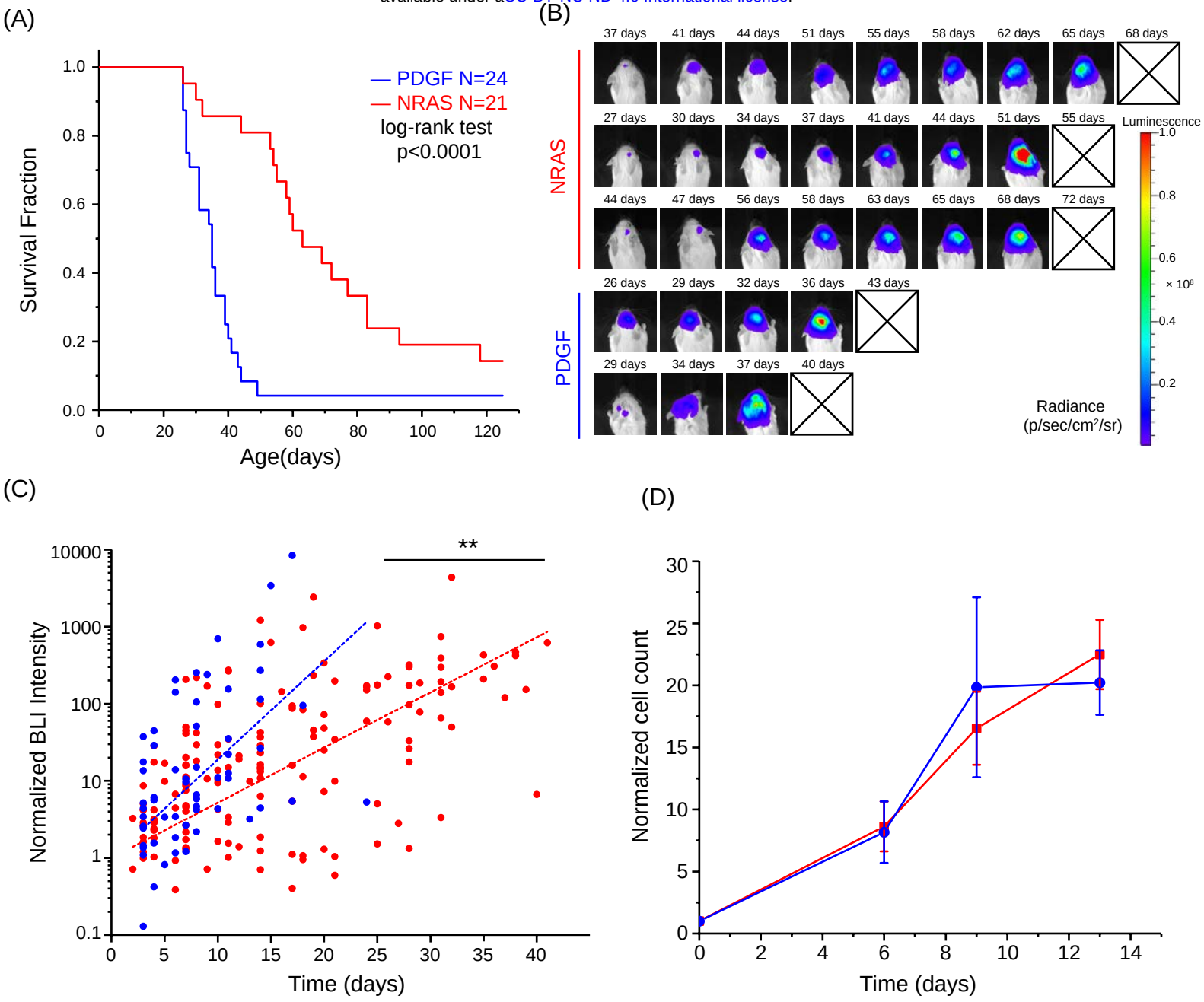

Figure 7

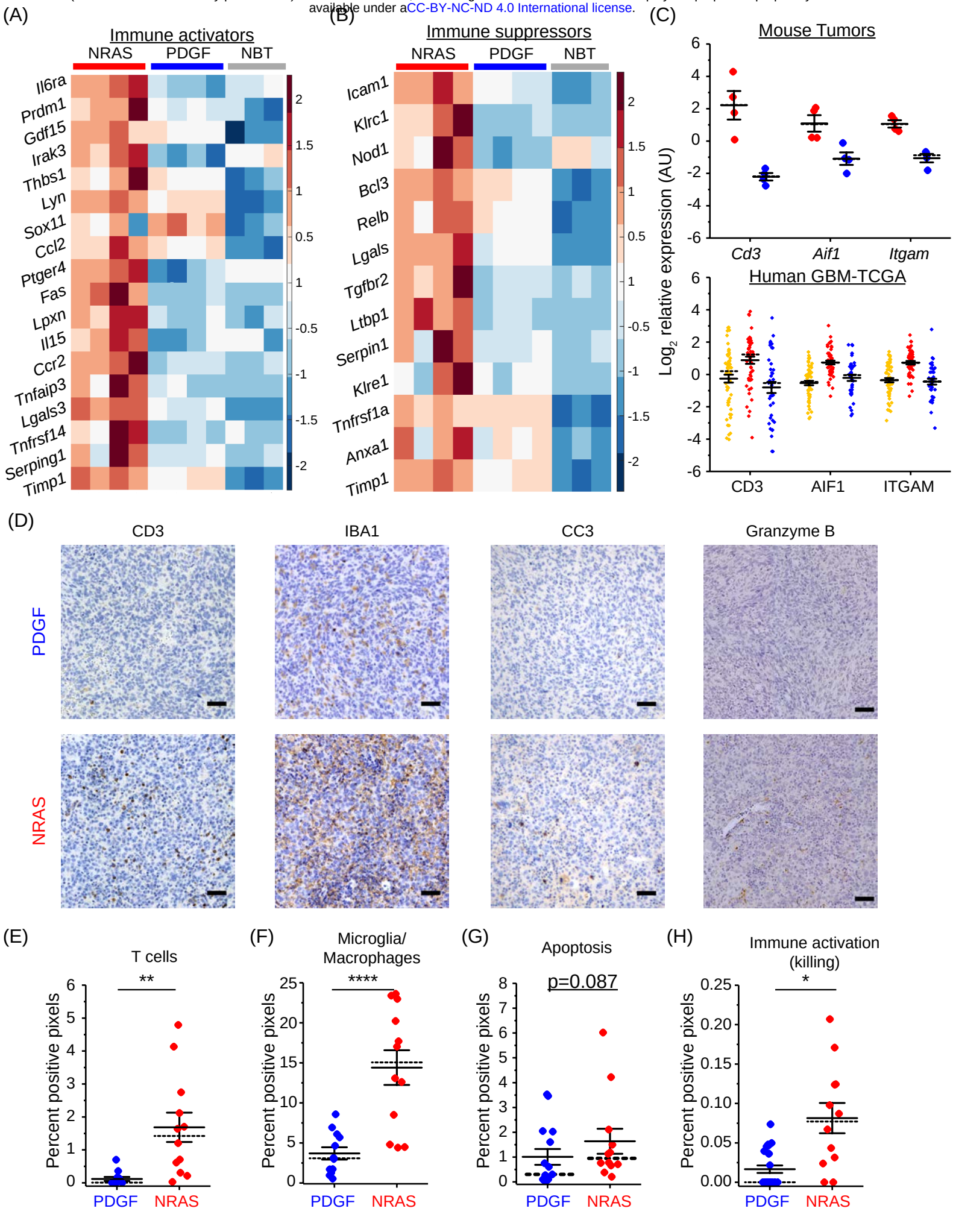

Figure 8

(A)

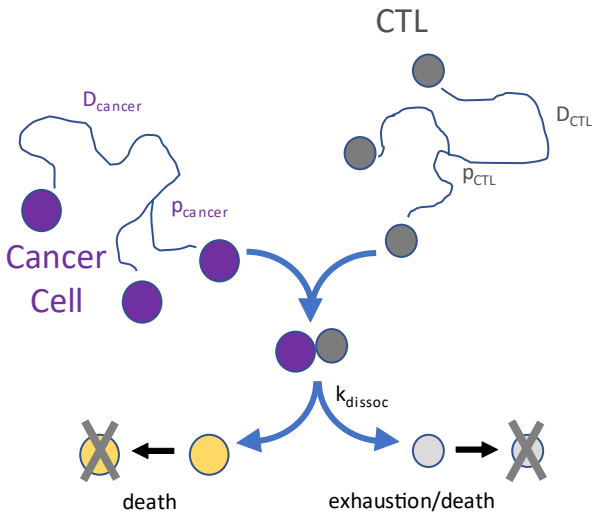

(B)

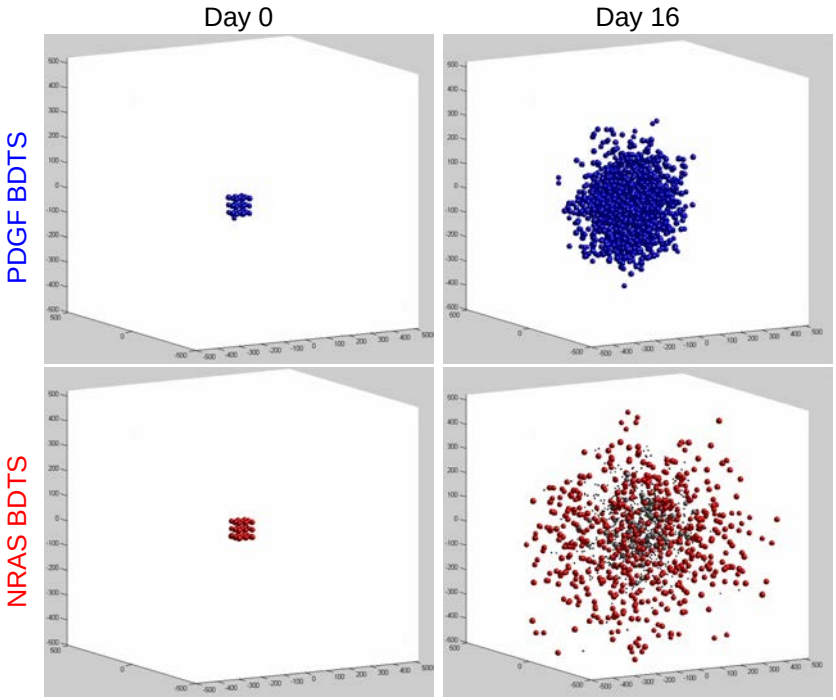

(C)

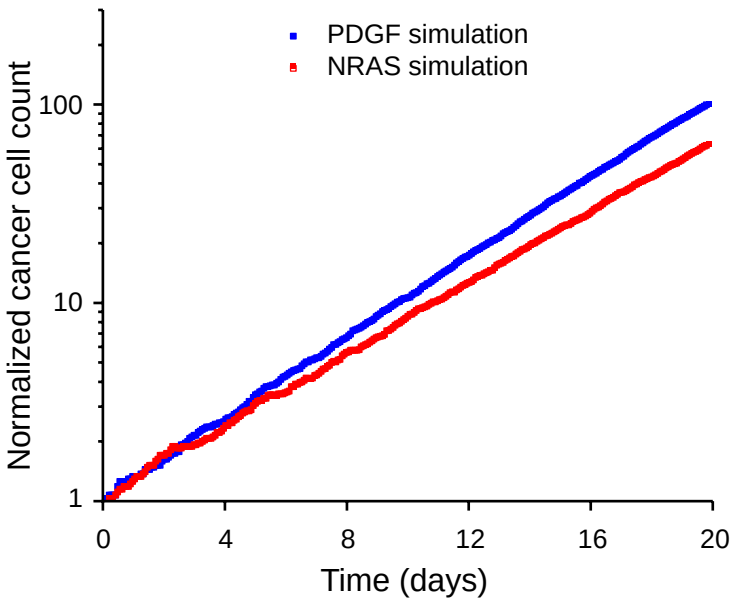

(D)

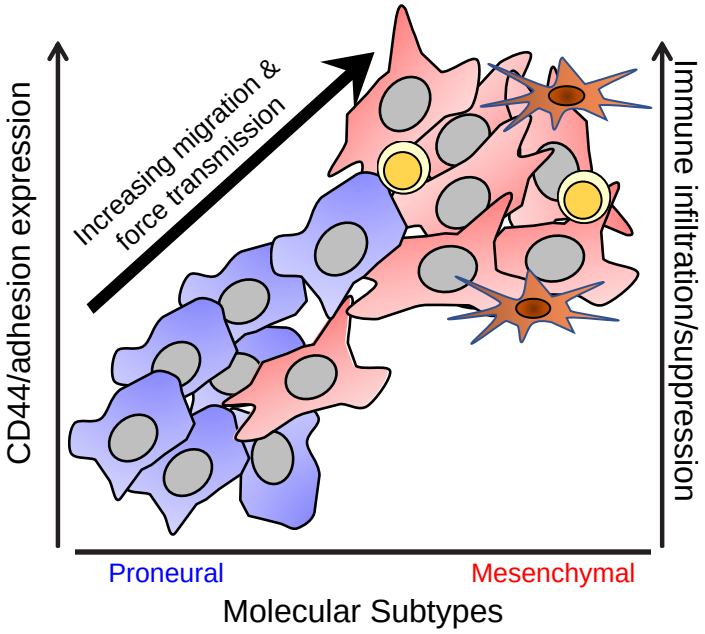

Figure S1

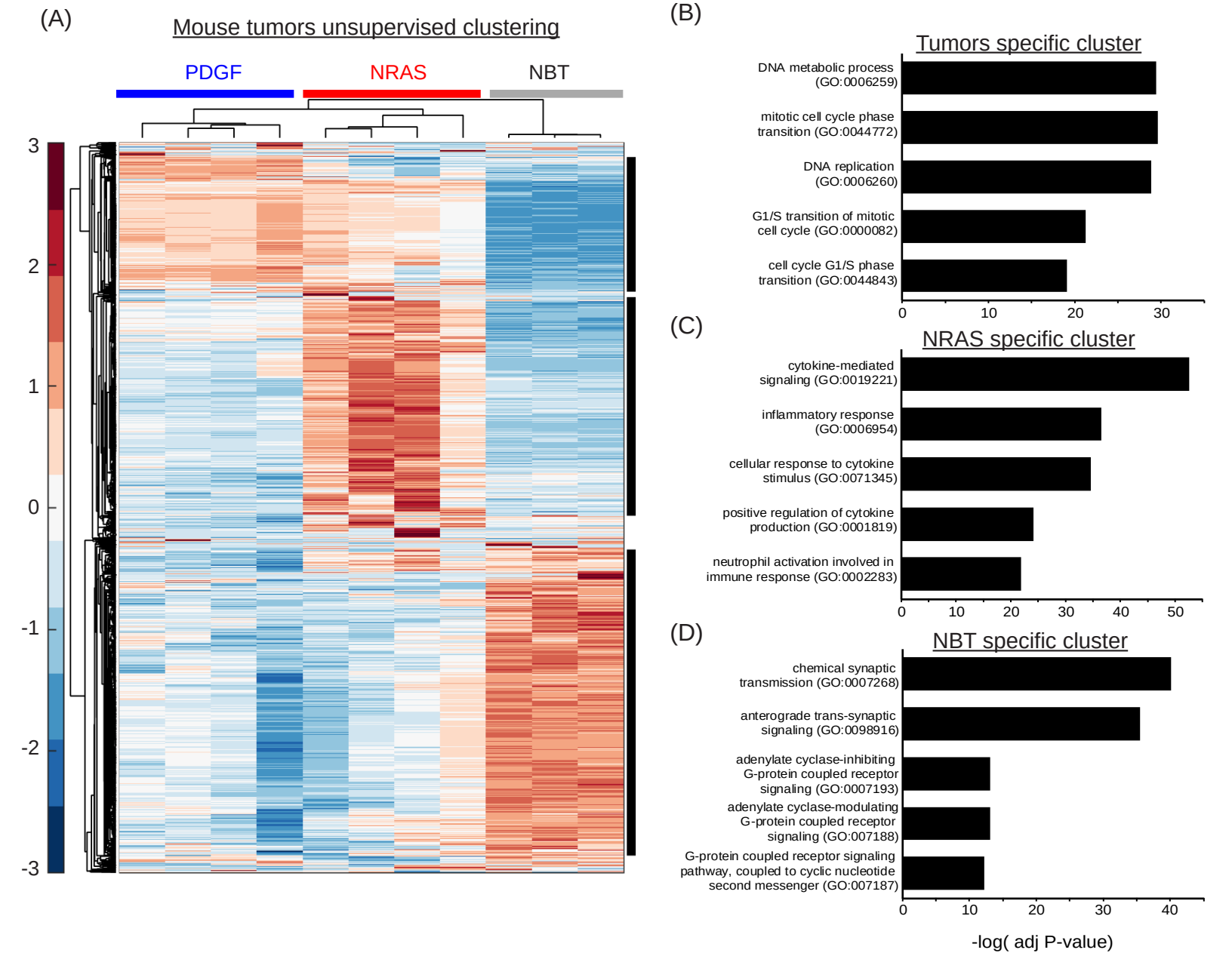

Figure S2

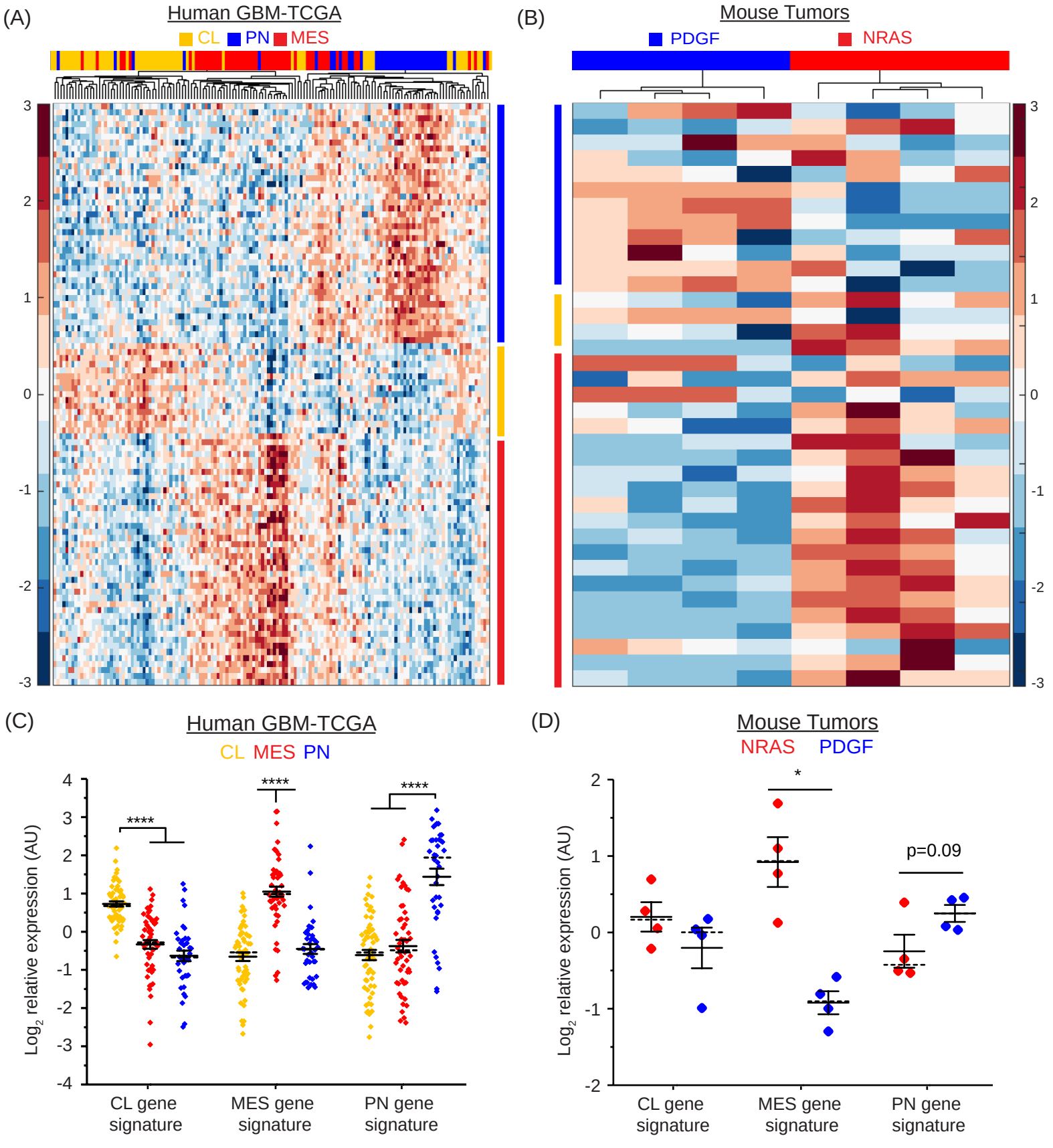

Figure S3

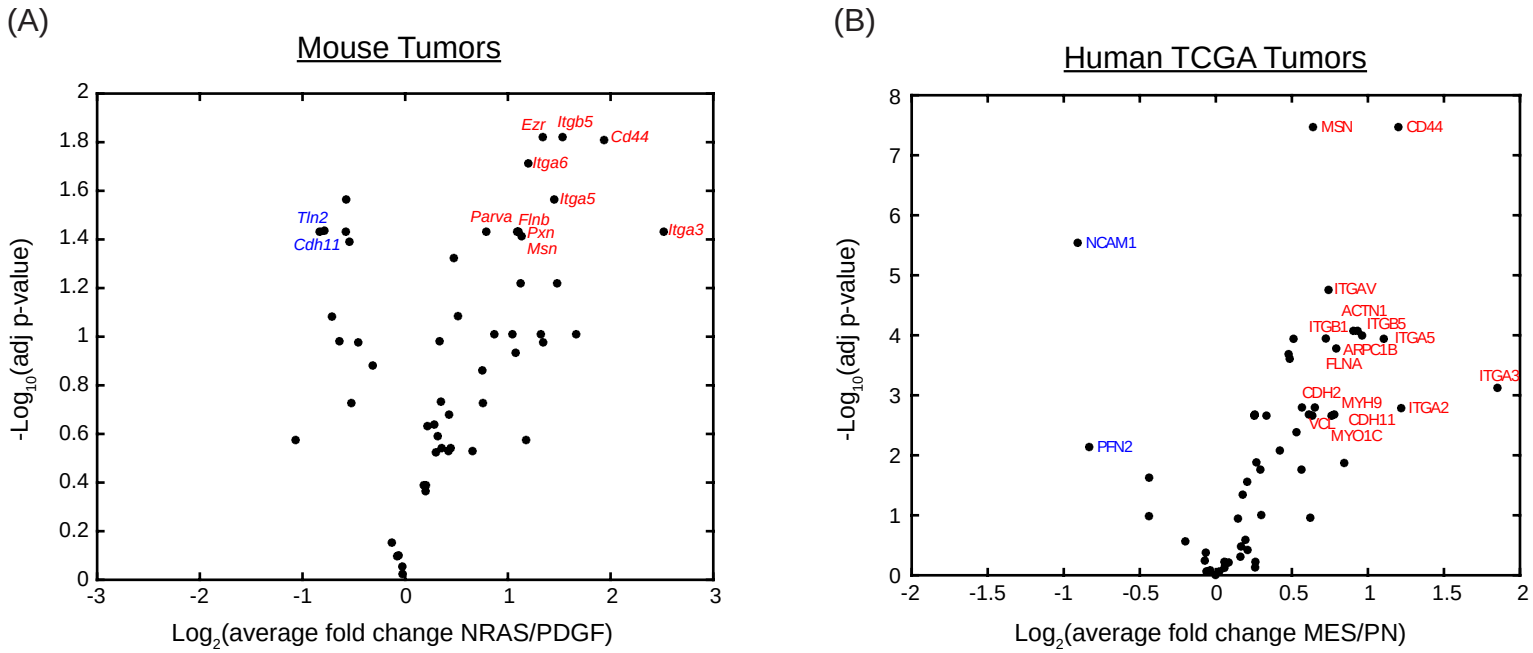

Figure S4

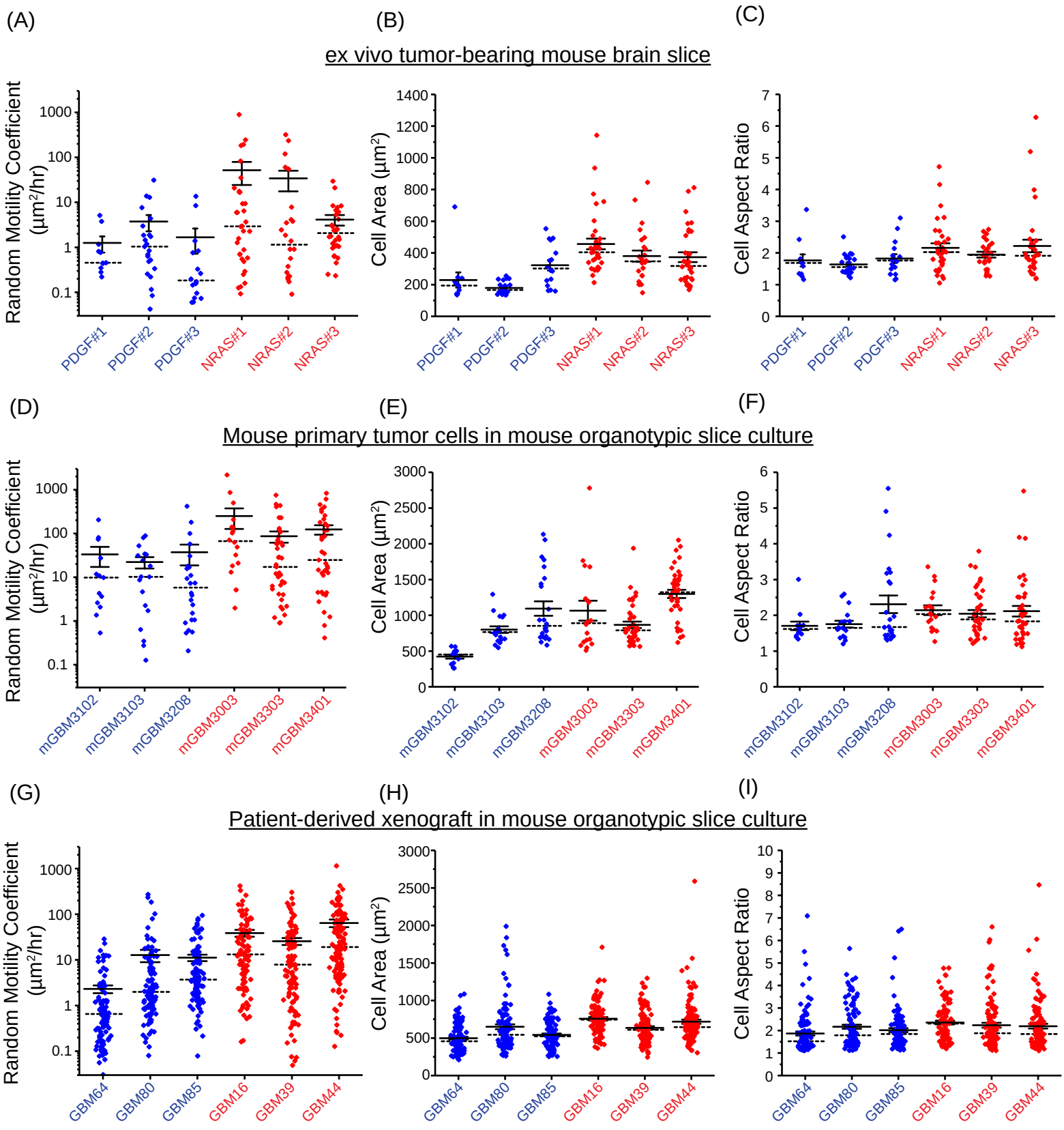

Figure S5

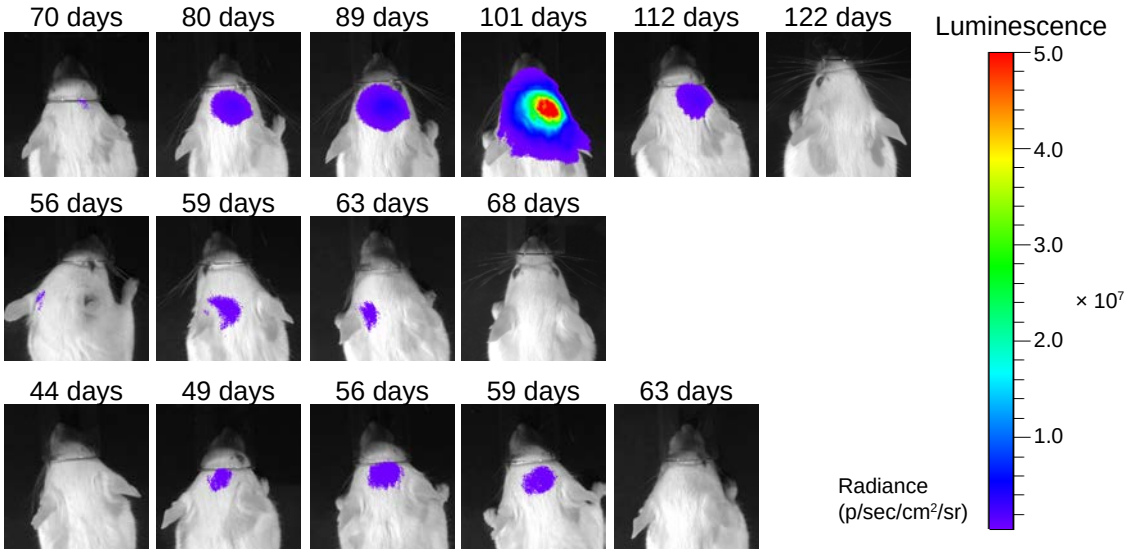

Figure S6